

Why adversarial training can hurt robust accuracy

Jacob Clarysse, Julia Hörrmann, and Fanny Yang

Department of Computer Science, ETH Zürich

Abstract

Machine learning classifiers with high test accuracy often perform poorly under adversarial attacks. It is commonly believed that adversarial training alleviates this issue. In this paper, we demonstrate that, surprisingly, the opposite may be true — Even though adversarial training helps when enough data is available, it may hurt robust generalization in the small sample size regime. We first prove this phenomenon for a high-dimensional linear classification setting with noiseless observations. Our proof provides explanatory insights that may also transfer to feature learning models. Further, we observe in experiments on standard image datasets that the same behavior occurs for perceptible attacks that effectively reduce class information such as mask attacks and object corruptions.

1 Introduction

Today’s best-performing classifiers are vulnerable to adversarial attacks [17, 46] and exhibit high *robust error*: for many inputs, their predictions change under adversarial perturbations, even though the true class stays the same. For example, in image classification tasks, we distinguish between two categories of such attacks that are content-preserving [16] (or consistent [38]) if their strength is limited — perceptible and imperceptible perturbations. Most work to date studies imperceptible attacks such as bounded ℓ_p -norm perturbations [17, 30, 32], small transformations using image processing techniques [15, 23, 29, 58] or nearby samples on the data manifold [27, 60]. They can often use their limited budget to successfully fool a learned classifier but, by definition, do not visibly reduce information about the actual class: the object in the perturbed image looks exactly the same as in the original version.

On the other hand, perceptible perturbations may occur more naturally in practice or are physically realizable. For example, stickers can be placed on traffic signs [14], masks of different sizes may cover important features of human faces [52], images might be rotated or translated [13], animals in motion may appear blurred in photographs depending on the shutter speed, or the lighting conditions could be poor (see Figure 2). Some perceptible attacks can effectively use the perturbation budget to reduce actual class information in the input (the *signal*) while still preserving the original class. For example, a stop sign with a small sticker doesn’t lose its semantic meaning or a flying bird does not become a different species because it induces motion blur in the image. We refer to these attacks as *directed attacks* (see Section 2 for a more formal characterization).

In this paper, we demonstrate that one of the most common beliefs for adversarial attacks does not transfer to directed attacks, in particular when the sample size is small. Specifically, it is widely acknowledged that

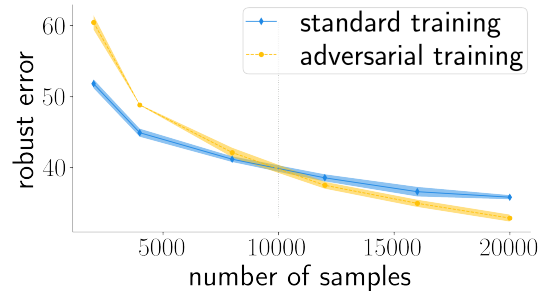


Figure 1: On subsampled CIFAR10 attacked by 2×2 masks, adversarial training yields higher robust error than standard training when the sample size is small, even though it helps for large sample sizes. (see Sec. E for details).

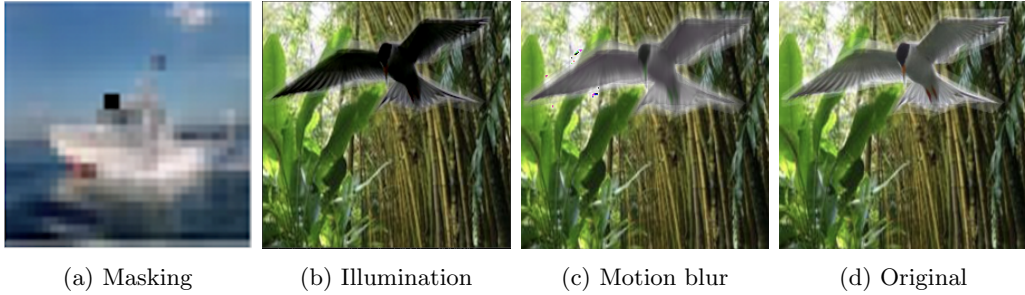


Figure 2: Examples of directed attacks on CIFAR10 and the Waterbirds dataset. In Figure 2a, we corrupt the image with a black mask of size 2×2 and in Figure 2b and 2c we change the lighting conditions (darkening) and apply motion blur on the bird in the image respectively. All perturbations effectively reduce the information about the class in the images: they are the result of directed attacks.

adversarial training often achieves significantly lower adversarial error than standard training. This holds in particular if the perturbation type [3, 30, 57] and perturbation budget match the attack during test time. Intuitively, the improvement is a result of decreased *attack-susceptibility*: independent of the true class, adversarial training explicitly encourages the classifier to predict the same class for all perturbed points.

In this paper, we question the efficacy of adversarial training to increase robust accuracy for directed attacks. In particular, we show that adversarial training not only increases standard test error as noted in [38, 45, 48, 57]), but surprisingly,

adversarial training may even increase the robust test error compared to standard training!

Figure 1 illustrates the main message of our paper for CIFAR10 subsets: Although adversarial training outperforms standard training when enough training samples are available, it is inferior in the low-sample regime. More specifically, our contributions are as follows:

- We prove that, almost surely, adversarially training a linear classifier on separable data yields a monotonically increasing robust error as the perturbation budget grows. We further establish high-probability non-asymptotic lower bounds on the robust error gap between adversarial and standard training.
- Our proof provides intuition for why this phenomenon is particularly prominent for directed attacks in the small sample size regime.
- We show that this phenomenon occurs on a variety of real-world datasets and perceptible directed attacks in the small sample size regime.

2 Robust classification

We first introduce our robust classification setting more formally by defining the notions of adversarial robustness, directed attacks and adversarial training used throughout the paper.

Adversarially robust classifiers For inputs $x \in \mathbb{R}^d$, we consider multi-class classifiers associated with parameterized functions $f_\theta : \mathbb{R}^d \rightarrow \mathbb{R}^K$, where K is the number of labels. In the special case of binary

classification ($K = 2$), we use the output predictions $y = \text{sign}(f_\theta(x))$. For example, $f_\theta(x)$ could be linear models (as in Section 3) or neural networks (as in Section 4).

One key step to encourage deployment of machine learning based classification in real-world applications, is to increase the robustness of classifiers against perturbations that do not change the ground truth label. Mathematically speaking, we would like to have a small ϵ_{te} -robust error, defined as

$$\text{Err}(\theta; \epsilon_{\text{te}}) := \mathbb{E}_{(x,y) \sim \mathbb{P}} \max_{x' \in T(x; \epsilon_{\text{te}})} \ell(f_\theta(x'), y), \quad (1)$$

where ℓ is the multi-class zero-one loss, which only equals 1 if the predicted output using $f_\theta(x)$ does not match the true label y . Further, $T(x; \epsilon_{\text{te}})$ is a perturbation set associated with a *transformation type* and size ϵ_{te} . Note that the (*standard*) error of a classifier corresponds to evaluating $\text{Err}(\theta; \epsilon_{\text{te}})$ at $\epsilon_{\text{te}} = 0$, yielding the standard error $\text{Err}(\theta; 0) = \mathbb{E}_{(x,y) \sim \mathbb{P}} \ell(f_\theta(x), y)$.

(Signal)-Directed attacks Most works in the existing literature consider consistent perturbations where ϵ_{te} is small enough such that all samples in the perturbation set have the same ground truth or expert label. Note that the ground truth model f_{θ^*} is therefore robust against perturbations and achieves the same error for standard and adversarial evaluation. The inner maximization in Equation (1) is often called the adversarial *attack* of the model f_θ and the corresponding solution is referred to as the adversarial example. In this paper, we consider *directed attacks*, as described in Section 1, that effectively reduce the information about the ground truth classes. Formally, we characterize *directed attacks* by the following property: for any model f_θ with low standard error, the corresponding adversarial example is well-aligned with the adversarial example found using the ground truth model f_{θ^*} . An example for such an attack are additive perturbations that are constrained to the direction of the ground truth decision boundary. We provide concrete examples for linear classification in Section 3.1.

Adversarial training In order to obtain classifiers with a good robust accuracy, it is common practice to minimize a (robust) training objective $\mathcal{L}_{\epsilon_{\text{tr}}}$ with a surrogate classification loss L such as

$$\mathcal{L}_{\epsilon_{\text{tr}}}(\theta) := \frac{1}{n} \sum_{i=1}^n \max_{x'_i \in T(x_i; \epsilon_{\text{tr}})} L(f_\theta(x'_i) y_i), \quad (2)$$

which is called adversarial training. In practice, we often use the cross entropy loss $L(z) = \log(1 + e^{-z})$ and minimize the robust objective by using first order optimization methods such as (stochastic) gradient descent. SGD is also the algorithm that we focus on in both the theoretical and experimental sections.

When the desired type of robustness is known in advance, it is standard practice to use the same perturbation set for training as for testing, i.e. $T(x; \epsilon_{\text{tr}}) = T(x; \epsilon_{\text{te}})$. For example, Madry et al. [30] shows that the robust error sharply increases for $\epsilon_{\text{tr}} < \epsilon_{\text{te}}$. In this paper, we show that for directed attacks in the small sample size regime, in fact, the opposite is true.

3 Theoretical results

In this section, we prove for linear functions $f_\theta(x) = \theta^\top x$ that in the case of directed attacks, robust generalization deteriorates with increasing ϵ_{tr} . The proof, albeit in a simple setting, provides explanations for why adversarial training fails in the high-dimensional regime for such attacks.

3.1 Setting

We now introduce the precise linear setting used in our theoretical results.

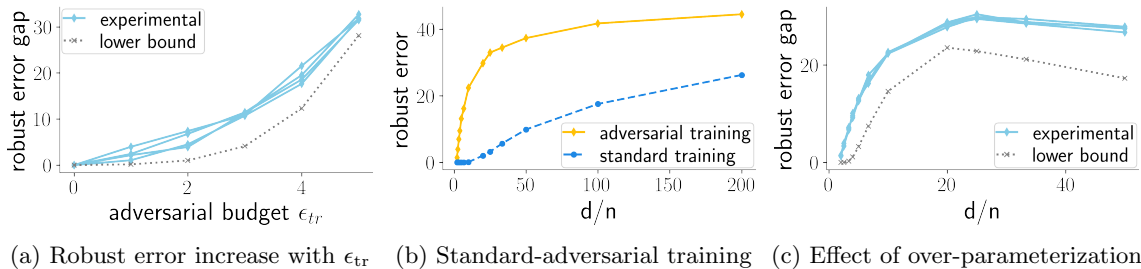


Figure 3: Experimental verification of Theorem 3.1. (a) We set $d = 1000$, $r = 12$, $n = 50$ and plot the robust error gap between standard and adversarial training with increasing adversarial budget ϵ_{tr} of 5 independent experiments. For comparison, we also plot the lower bound given in Theorem 3.1. In (b) and (c), we set $d = 10000$ and vary the number of samples n . (b) We plot the robust error of standard and adversarial training ($\epsilon_{tr} = 4.5$). (c) We compute the error gap and the lower bound of Theorem 3.1. For more experimental details see Appendix C.

Data model In this section, we assume that the ground truth and hypothesis class are given by linear functions $f_\theta(x) = \theta^\top x$ and the sample size n is lower than the ambient dimension d . In particular, the generative distribution \mathbb{P}_r is similar to [35, 48]: The label $y \in \{+1, -1\}$ is drawn with equal probability and the covariate vector is sampled as $x = [y \frac{r}{2}, \tilde{x}]$ with the random vector $\tilde{x} \in \mathbb{R}^{d-1}$ drawn from a standard normal distribution, i.e. $\tilde{x} \sim \mathcal{N}(0, \sigma^2 I_{d-1})$. We would like to learn a classifier that has low robust error by using a dataset $D = (x_i, y_i)_{i=1}^n$ with n i.i.d. samples from \mathbb{P}_r .

Notice that the distribution \mathbb{P}_r is noiseless: for a given input x , the label $y = \text{sign}(x_{[1]})$ is deterministic. Further, the optimal linear classifier (also referred to as the *ground truth*) is parameterized by $\theta^* = e_1$.¹ By definition, the ground truth is robust against all consistent perturbations and hence the optimal robust classifier.

Directed attacks The focus in this paper lies on consistent directed attacks that by definition efficiently concentrate their attack budget in the direction of the signal. For our linear setting, we can model such attacks by additive perturbations in the first dimension

$$T(x; \epsilon) = \{x' = x + \delta \mid \delta = \beta e_1 \text{ and } -\epsilon \leq \beta \leq \epsilon\}. \quad (3)$$

Note that this attack is always in the direction of the true signal dimension, i.e. the ground truth. Furthermore, when $\epsilon < \frac{r}{2}$, it is a consistent directed attack. Observe how this is different from ℓ_p attacks - an ℓ_p attack, depending on the model, may add a perturbation that only has a very small component in the signal direction.

Robust max- ℓ_2 -margin classifier A long line of work studies the implicit bias of interpolators that result from applying stochastic gradient descent on the logistic loss until convergence [9, 21, 28, 34]. For linear models, we obtain the ϵ_{tr} -robust maximum- ℓ_2 -margin solution (*robust max-margin* in short)

$$\hat{\theta}^{\epsilon_{tr}} := \arg \max_{\|\theta\|_2 \leq 1} \min_{i \in [n], x'_i \in T(x_i; \epsilon_{tr})} y_i \theta^\top x'_i. \quad (4)$$

This can for example be shown by a simple rescaling argument using Theorem 3.4 in [28]. Even though our result is proven for the max- ℓ_2 -margin classifier, it can easily be extended to other interpolators.

¹Note that the result more generally holds for non-sparse models that are not axis aligned by way of a simple rotation $z = Ux$. In that case the distribution is characterized by $\theta^* = u_1$ and a rotated Gaussian in the $d - 1$ dimensions orthogonal to θ^* .

3.2 Main results

We are now ready to characterize the ϵ_{te} -robust error as a function of ϵ_{tr} , the separation r , the dimension d and sample size n of the data. In the theorem statement we use the following quantities

$$\begin{aligned}\varphi_{\min} &= \frac{\sigma}{r/2 - \epsilon_{te}} \left(\sqrt{\frac{d-1}{n}} - \left(1 + \sqrt{\frac{2 \log(2/\delta)}{n}} \right) \right) \\ \varphi_{\max} &= \frac{\sigma}{r/2 - \epsilon_{te}} \left(\sqrt{\frac{d-1}{n}} + \left(1 + \sqrt{\frac{2 \log(2/\delta)}{n}} \right) \right)\end{aligned}$$

that arise from concentration bounds for the singular values of the random data matrix. Further, let $\tilde{\epsilon} := \frac{r}{2} - \frac{\varphi_{\max}}{\sqrt{2}}$ and denote by Φ the cumulative distribution function of a standard normal.

Theorem 3.1. *Assume $d-1 > n$. For any $\epsilon_{te} \geq 0$, the ϵ_{te} -robust error on test samples from \mathbb{P}_r with $2\epsilon_{te} < r$ and perturbation sets in Equation (3) and (9), the following holds:*

1. *The ϵ_{te} -robust error of the ϵ_{tr} -robust max-margin estimator reads*

$$\text{Err}(\hat{\theta}^{\epsilon_{tr}}; \epsilon_{te}) = \Phi \left(-\frac{\left(\frac{r}{2} - \epsilon_{tr}\right)}{\tilde{\varphi}} \right) \quad (5)$$

for a random quantity $\tilde{\varphi} > 0$ depending on σ, r, ϵ_{te} , which is a strictly increasing function with respect to ϵ_{tr} .

2. *With probability at least $1 - \delta$, we further have $\varphi_{\min} \leq \tilde{\varphi} \leq \varphi_{\max}$ and the following lower bound on the robust error increase by adversarially training with size ϵ_{tr}*

$$\text{Err}(\hat{\theta}^{\epsilon_{tr}}; \epsilon_{te}) - \text{Err}(\hat{\theta}^0; \epsilon_{te}) \geq \Phi \left(\frac{r/2}{\varphi_{\min}} \right) - \Phi \left(\frac{r/2 - \min\{\epsilon_{tr}, \tilde{\epsilon}\}}{\varphi_{\min}} \right). \quad (6)$$

The proof can be found in Appendix A and primarily relies on high-dimensional probability. Note that the theorem holds for any $0 \leq \epsilon_{te} < \frac{r}{2}$ and hence also directly applies to the standard error by setting $\epsilon_{te} = 0$. In Figure 3, we empirically confirm the statements of Theorem 3.1 by performing multiple experiments on synthetic datasets as described in Subsection 3.1 with different choices of d/n and ϵ_{tr} . In the first statement, we prove that for small sample-size ($n < d-1$) noiseless data, almost surely, the robust error increases monotonically with adversarial training budget $\epsilon_{tr} > 0$. In Figure 3a, we plot the robust error gap between standard and adversarial logistic regression in function of the adversarial training budget ϵ_{tr} for 5 runs.

The second statement establishes a simplified lower bound on the robust error increase for adversarial training (for a fixed $\epsilon_{tr} = \epsilon_{te}$) compared to standard training. In Figures 3a and 3c, we show how the lower bound closely predicts the robust error gap in our synthetic experiments. Furthermore, by the dependence of φ_{\min} on the overparameterization ratio d/n , the lower bound on the robust error gap is amplified for large d/n . Indeed, Figure 3c shows how the error gap increases with d/n both theoretically and experimentally. However, when d/n increases above a certain threshold, the gap decreases again, as standard training fails to learn the signal and yields a high error (see Figure 3b).

3.3 Proof idea: intuition and surprises

The reason that adversarial training hurts robust generalization is based on an extreme robust vs. standard error tradeoff. We provide intuition for the effect of directed attacks and the small sample regime on the solution of adversarial training by decomposing the robust error $\text{Err}(\theta; \epsilon_{te})$. Notice that ϵ_{te} -robust error

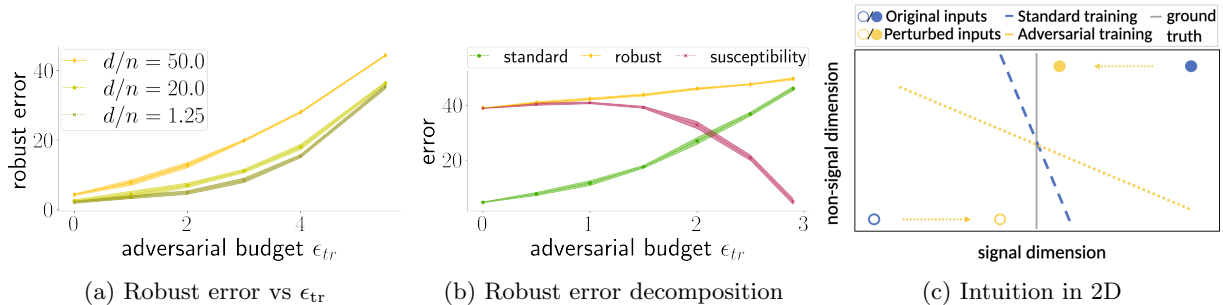


Figure 4: (a) We set $d = 1000$ and $r = 12$ and plot the robust error with increasing adversarial training budget (ϵ_{tr}) and with increasing d/n . (b) We plot the robust error decomposition in susceptibility and standard error for increasing adversarial budget ϵ_{tr} . Full experimental details can be found in Section C. (c) 2D illustration providing intuition for the linear setting: Training on directed attacks (yellow) effectively corresponds to fitting the original datapoints (blue) after shifting them closer to the decision boundary. The robust max- ℓ_2 -margin (yellow dotted) is heavily tilted if the points are far apart in the non-signal dimension, while the standard max- ℓ_2 -margin solution (blue dashed) is much closer to the ground truth (gray solid).

$\text{Err}(\theta; \epsilon_{te})$ can be written as the probability of the union of two events: the event that the classifier based on θ is wrong and the event that the classifier is susceptible to attacks:

$$\begin{aligned} \text{Err}(\theta; \epsilon_{te}) &= \mathbb{E}_{x, y \sim \mathbb{P}} \left[\mathbb{I}\{y f_{\theta}(x) < 0\} \vee \max_{x' \in T(x; \epsilon_{te})} \mathbb{I}\{f_{\theta}(x) f_{\theta}(x') < 0\} \right] \\ &\leq \text{Err}(\theta; 0) + \text{Sus}(\theta; \epsilon_{te}) \end{aligned} \quad (7)$$

where $\text{Sus}(\theta; \epsilon_{te})$ is the expectation of the maximization term in Equation (7). $\text{Sus}(\theta; \epsilon_{te})$ represents the ϵ_{tr} -*attack-susceptibility* of a classifier induced by θ and $\text{Err}(\theta; 0)$ its standard error. Equation (7) suggests that the robust error can only be small if both the standard error and susceptibility are small. In Figure 4b, we plot the decomposition of the robust error in standard error and susceptibility for adversarial logistic regression with increasing ϵ_{tr} . We observe that increasing ϵ_{tr} increases the standard error too drastically compared to the decrease in susceptibility, leading to an effective drop in robust accuracy. For completeness, in Appendix B, we provide upper and lower bounds for the susceptibility score. We now explain why, in the small-sample size regime, adversarial training with directed attacks (3) may increase standard error to the extent that it dominates the decrease in susceptibility.

A key observation is that the robust max- ℓ_2 -margin solution of a dataset $D = \{(x_i, y_i)\}_{i=1}^n$ maximizes the minimum margin that reads $\min_{i \in [n]} y_i \theta^{\top} (x_i - y_i \epsilon_{tr} |_{\theta_{[1]}} e_1)$, where $\theta_{[i]}$ refers to the i -th entry of vector θ . Therefore, it simply corresponds to the max ℓ_2 -margin solution of the dataset shifted towards the decision boundary $D_{\epsilon_{tr}} = \{(x_i - y_i \epsilon_{tr} |_{\hat{\theta}_{[1]}^{\epsilon_{tr}}} e_1, y_i)\}_{i=1}^n$. Using this fact, we obtain a closed-form expression of the (normalized) max-margin solution (4) as a function of ϵ_{tr} that reads

$$\hat{\theta}^{\epsilon_{tr}} = \frac{1}{(r - 2\epsilon_{tr})^2 + 4\tilde{\gamma}^2} \left[r - 2\epsilon_{tr}, 2\tilde{\gamma}\tilde{\theta} \right], \quad (8)$$

where $\|\tilde{\theta}\|_2 = 1$ and $\tilde{\gamma} > 0$ is a random quantity associated with the max- ℓ_2 -margin solution of the $d - 1$ dimensional Gaussian inputs orthogonal to the signal direction (see Lemma A.1 in Section A).

In high dimensions, with high probability any two Gaussian random vectors are far apart – in our distributional setting, this corresponds to the vectors being far apart in the non-signal directions. In Figure 4c, we illustrate the phenomenon using a simplified 2D cartoon, where the few samples in the dataset are all far apart in the non-signal direction. We see how shifting the dataset closer to the true decision boundary, may result in a max-margin solution (yellow) that aligns much worse with the ground truth (gray), compared to the estimator

learned from the original points (blue). Even though the new (robust max-margin) classifier (yellow) is less susceptible to directed attacks in the signal dimension, it also uses the signal dimension less. Mathematically, this is directly reflected in the expression of the max-margin solution in Equation (8): Even without the definition of $\tilde{\gamma}, \tilde{\theta}$, we can directly see that the first (signal) dimension is used less as ϵ_{tr} increases.

3.4 Generality of the results

In this section we discuss how the theorem might generalize to other perturbation sets, models and training procedures.

Signal direction is known The type of additive perturbations used in Theorem 3.1, defined in Equation (3), is explicitly constrained to the direction of the true signal. This choice is reminiscent of corruptions where every possible perturbation in the set is directly targeted at the object to be recognized, such as motion blur of moving objects. Such corruptions are also studied in the context of domain generalization and adaptation [43].

Directed attacks in general, however, may also consist of perturbation sets that are only strongly biased towards the true signal direction, such as mask attacks. They may find the true signal direction only when the inner maximization is exact. The following corollary extends Theorem 3.1 to small ℓ_1 -perturbations

$$T(x; \epsilon) = \{x' = x + \delta \mid \|\delta\|_1 \leq \epsilon\}, \quad (9)$$

for $0 < \epsilon < \frac{\tau}{2}$ that reflect such attacks. We state the corollary here and give the proof in Appendix A.

Corollary 3.2. *Theorem 3.1 also holds for (4) with perturbation sets defined in (9).*

The proof uses the fact that the inner maximization effectively results in a sparse perturbation equivalent to the attack resulting from the perturbation set (3).

Other models Motivated by the implicit bias results of (stochastic) gradient descent on the logistic loss, Theorem 3.1 is proven for the max- ℓ_2 -margin solution. We would like to conjecture that for the data distribution in Section 3, adversarial training can hurt robust generalization also for other models with zero training error (*interpolators* in short).

For example, Adaboost is a widely used algorithm that converges to the max- ℓ_1 -margin classifier [47]. One might argue that for a sparse ground truth, the max- ℓ_1 -margin classifier should (at least in the noiseless case) have the right inductive bias to alleviate large bias in high dimensions. Hence, in many cases the (sparse) max- ℓ_1 -margin solution might align with the ground truth for a given dataset. However, we conjecture that even in this case, the *robust* max- ℓ_1 -margin solution (of the dataset shifted towards the decision boundary) would be misled to choose a wrong sparse solution. This can be seen with the help of the cartoon illustration in Figure 4c.

4 Real-world experiments

In this section, we demonstrate that adversarial training may hurt robust accuracy in a variety of image attack scenarios on the Waterbirds and CIFAR10 dataset. The corresponding experimental details and more experimental results (including on an additional hand gestures dataset) can be found in Appendices D, E and F.

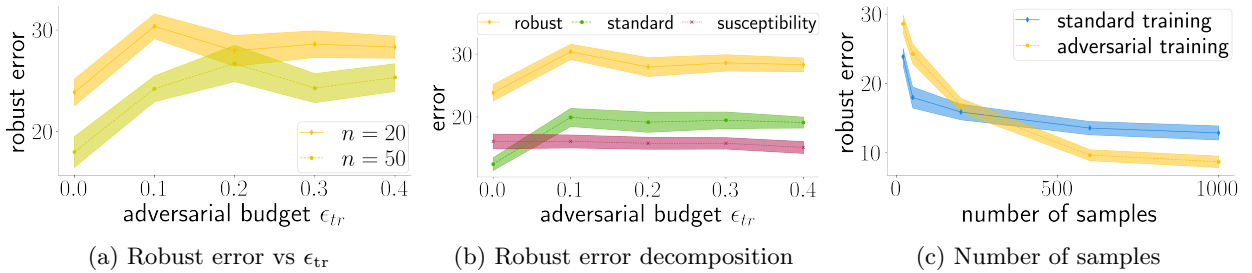


Figure 5: Experiments on the Waterbirds dataset considering the adversarial illumination attack with $\epsilon_{te} = 0.3$. We plot the mean and standard deviation of the mean of several independent experiments. (a) The robust error increases with larger ϵ_{tr} in the low sample size regime. (b) We set $n = 20$ and plot the robust error decomposition as in Equation (7) with increasing ϵ_{tr} . While the susceptibility decreases slightly, the increase in standard error is much more severe, resulting in an increase in robust error. (c) Adversarial training hurts robust generalization in the low sample size regime ($n < 200$), but helps when enough samples are available. For more experimental details see Section D.

4.1 Datasets

We now describe the datasets and models that we use for the experiments. In all our experiments on CIFAR10, we vary the sample size by subsampling the dataset and use a ResNet18 [18] as model. We always train on the same (randomly subsampled) dataset, meaning that the variances arise from the random seed of the model and the randomness in the training algorithm. In Appendix E, we complement the results of this section by reporting the results of similar experiments with different architectures.

As a second dataset, we build a new version of the Waterbirds dataset, consisting of images of water- and landbirds of size 256×256 and labels that distinguish the two types of birds. We construct the dataset as follows: First, we sample equally many water- and landbirds from the CUB-200 dataset [50]. Then, we segment the birds and paste them onto a background that is randomly sampled (without replacement) from the Places-256 dataset [59]. For the implementation of the dataset we used the code provided by Sagawa* et al. [40]. Also, following the choice of Sagawa* et al. [40], we use as model a ResNet50 that was pretrained on ImageNet and which achieves near perfect standard accuracy.

4.2 Evaluation of directed attacks

We consider three types of directed attacks on our real world datasets: square masks, motion blur and adversarial illumination. The mask attack is a model used to simulate sticker-attacks and general occlusions of objects in images [14, 52]. On the other hand, motion blur may arise naturally for example when photographing fast moving objects with a slow shutter speed. Further, adversarial illumination may result from adversarial lighting conditions or smart image corruptions. Next, we describe the attacks in more detail.

Mask attacks On CIFAR10, we consider the square black mask attack: the adversary can set a mask of size $\epsilon_{te} \times \epsilon_{te}$ to zero in the image. To ensure that the mask does not cover the whole signal in the image, we restrict the size of the masks to be at most 2×2 . Hence, the search space of the attack consists of all possible locations of the masks in the targeted image. For exact robust error evaluation, we perform a full grid search over all possible locations during test time. See Figure 2a for an example of a mask attack on CIFAR10.

Motion blur On the Waterbirds dataset we consider two directed attacks: motion blur and adversarial illumination. For the motion blur attack, the bird may move at different speeds without changing the background. The aim is to be robust against all motion blur severity levels up to $M_{max} = 15$. To simulate motion blur, we first segment the birds and then use a filter with a kernel of size M to apply motion blur on the bird only. Lastly, we paste the blurred bird back onto the background image. We can change the severity level of the motion blur by increasing the kernel size of the filter. See Appendix D for an ablation study and concrete expressions of the motion blur kernel. At test time, we perform a full grid search over all kernel sizes to exactly evaluate the robust error. We refer to Figure 2c and Section D for examples of our motion blur attack.

Adversarial illumination As a second attack on the Waterbirds dataset, we consider adversarial illumination. The adversary can darken or brighten the bird without corrupting the background of the image. The attack aims to model images where the object at interest is hidden in shadows or placed against bright light. To compute the adversarial illumination attack, we segment the bird, then darken or brighten the it, by adding a constant $a \in [-\epsilon_{te}, \epsilon_{te}]$, before pasting the bird back onto the background image. We find the most adversarial lighting level, i.e. the value of a , by equidistantly partitioning the interval $[-\epsilon_{te}, \epsilon_{te}]$ in K steps and performing a full list-search over all steps. See Figure 2b and Section D for examples of the adversarial illumination attack.

4.3 Adversarial training procedure

For all datasets, we run SGD until convergence on the *robust* cross-entropy loss (2). In each iteration, we search for an adversarial example and update the weights using a gradient with respect to the resulting perturbed example [17, 30]. For every experiment, we choose the learning rate and weight decay parameters that minimize the robust error on a hold-out dataset. We now describe the implementation of the adversarial search for the three types of directed attacks.

Mask attacks Unless specified otherwise, we use an approximate attack similar to Wu et al. [52] during training time: First, we identify promising mask locations by analyzing the gradient, $\nabla_x L(f_\theta(x), y)$, of the cross-entropy loss with respect to the input. Masks that cover part of the image where the gradient is large, are more likely to increase the loss. Hence, we compute the K mask locations (i, j) , where $\|\nabla_x L(f_\theta(x), y)_{[i:i+2, j:j+2]}\|_1$ is the largest and take using a full list-search the mask that incurs the highest loss. Our intuition from the theory predicts that higher K , and hence a more exact “defense”, only increases the robust error of adversarial training, since the mask could then more efficiently cover important information about the class. We indeed confirm this effect and provide more details in Section E.

Motion blur Intuitively the worst attack should be the most severe blur, rendering a search over a range of severity superfluous. However, similar to rotations, this is not necessarily true in practice since the training loss on neural networks is generally nonconvex. Hence, during training time, we perform a search over kernels with sizes $2i$ for $i = 1, \dots, M_{max}/2$. Note that, at test time, we do an exact search over all kernels of sizes in $[1, 2, \dots, M_{max}]$.

Adversarial illumination Similar to the motion blur attack, intuitively the worst perturbation should be the most severe lighting changes; either darkening or illuminating the object maximally. However, again this is not necessarily the case, since finding the worst attack is a nonconvex problem. Therefore, during training and testing we partition the interval $[-\epsilon_{tr}, \epsilon_{tr}]$ in 33 and 65 steps respectively, and perform a full grid-search to find the worst perturbation.

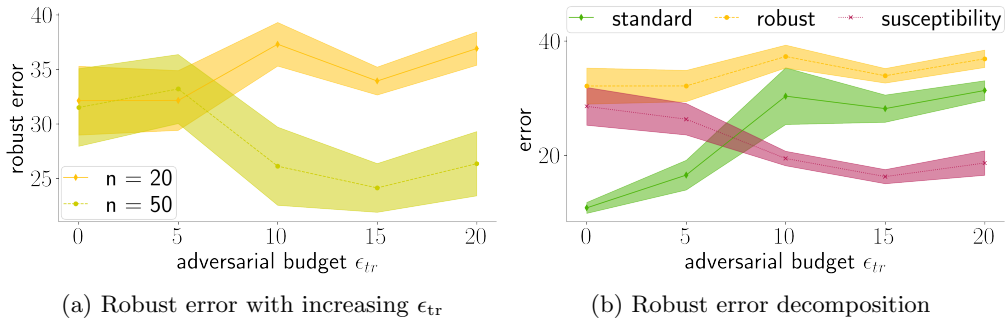


Figure 6: (a) We plot the robust error with increasing adversarial training budget ϵ_{tr} of 5 experiments on the subsampled Waterbirds datasets of sample sizes 20 and 30. Even though adversarial training hurts robust generalization for low sample size ($n = 20$), it helps for $n = 50$. (b) We plot the decomposition of the robust error in standard error and susceptibility with increasing adversarial budget ϵ_{tr} . We plot the mean and standard deviation of the mean of 5 experiments on a subsampled Waterbirds dataset of size $n = 20$. The increase in standard error is more severe than the drop in susceptibility, leading to a slight increase in robust error. For more experimental details see Section D.

4.4 Adversarial training can hurt robust generalization

Further, we perform the following experiments on the Waterbirds dataset using the motion blur and adversarial illumination attack. We vary the adversarial training budget ϵ_{tr} , while keeping the number of samples fixed, and compute the resulting robust error. We see in Figure 5a and 6a that, indeed, adversarial training can hurt robust generalization with increasing perturbation budget ϵ_{tr} .

Furthermore, to gain intuition as described in Section 3.3 and, we also plot the robust error decomposition (Equation 7) consisting of the standard error and susceptibility in Figure 5b and 6b. Recall that we measure susceptibility as the fraction of data points in the test set for which the classifier predicts a different class under an adversarial attack. As in our linear example, we observe an increase in robust error despite a slight drop in susceptibility, because of the more severe increase in standard error. Similar experiments for the hand gesture dataset can be found in F.

As predicted by our theorem, the phenomenon where adversarial training hurts robust generalization is most pronounced in the small sample size regime. Indeed, the experiments depicted in Figures 5a and 6a are conducted on small sample size datasets of $n = 20$ or 50. In Figure 1 and 5c, we observe that as sample size increases, adversarial training does improve robust generalization compared to standard training, even for directed attacks. Moreover, on the experiments of CIFAR10 using the mask perturbation, which can be found in Figure 1 and Appendix E, we observe the same behaviour: Adversarial training hurts robust generalization in the low sample size regime, but helps when enough samples are available.

4.5 Discussion

In this section, we discuss how different algorithmic choices, motivated by related work, affect when and how adversarial training hurts robust generalization.

Strength of attack and catastrophic overfitting In many cases, the worst case perturbation during adversarial training is found using an approximate algorithm such as projected gradient descent. It is common belief that using the strongest attack (in the mask-perturbation case, full grid search) during training should also result in better robust generalization. In particular, the literature on catastrophic overfitting shows that

weaker attacks during training lead to bad performance on stronger attacks during testing [2, 26, 51]. Our result suggests the opposite is true in the low-sample size regime for directed attacks: the weaker the attack, the better adversarial training performs.

Robust overfitting Recent work observes empirically [39] and theoretically [12, 41], that perfectly minimizing the adversarial loss during training might in fact be suboptimal for robust generalization; that is, classical regularization techniques might lead to higher robust accuracy. The phenomenon is often referred to as robust overfitting. May the phenomenon be mitigated using standard regularization techniques? In Appendix D we shed light on this question and show that adversarial training hurts robust generalization even with standard regularization methods such as early stopping are used.

5 Related work

We now discuss how our results relate to phenomena that have been observed or proven in the literature before.

Robust and non-robust useful features In the words of Ilyas et al. [19], Springer et al. [44], for directed attacks, all robust features become less useful, but adversarial training uses robust features more. In the small sample-size regime $n < d - 1$ in particular, robust learning assigns so much weight on the robust (possibly non-useful) features, that the signal in the non-robust features is drowned. This leads to an unavoidable and large increase in standard error that dominates the decrease in susceptibility and hence ultimately leads to an increase of the robust error.

Small sample size and robustness A direct consequence of Theorem 3.1 is that in order to achieve the same robust error as standard training, adversarial training requires more samples. This statement might remind the reader of sample complexity results for robust generalization in Khim & Loh [22], Schmidt et al. [42], Yin et al. [55]. While those results compare sample complexity bounds for standard vs. robust error, our theorem statement compares two algorithms, standard vs. adversarial training, with respect to the robust error.

Trade-off between standard and robust error Many papers observed that even though adversarial training decreases robust error compared to standard training, it may lead to an increase in standard test error [30, 57]. For example, Chen et al. [7], Dobriban et al. [11], Javanmard et al. [20], Tsipras et al. [48], Zhang et al. [57] study settings where the Bayes optimal robust classifier is not equal to the Bayes optimal (standard) classifier (i.e. the perturbations are inconsistent or the dataset is non-separable). [38] study consistent perturbations, as in our paper, and prove that for small sample size, fitting adversarial examples can increase standard error even in the absence of noise. In contrast to aforementioned works, which do not refute that adversarial training decreases robust error, we prove that for directed attacks perturbations, in the small sample regime adversarial training may also increase *robust error*.

Mitigation of the trade-off A long line of work has proposed procedures to mitigate the trade-off phenomenon. For example Alayrac et al. [1], Carmon et al. [6], Raghunathan et al. [38], Zhai et al. [56] study robust self training, which leverages a large set of unlabelled data, while Lamb et al. [24], Lee et al. [25], Xu et al. [53] use data augmentation by interpolation. Balaji et al. [4], Cheng et al. [8], Ding et al. [10] on the other hand propose to use adaptive perturbation budgets ϵ_{tr} that vary across inputs. Our intuition from the theoretical analysis suggests that the standard mitigation procedures for imperceptible perturbations may

not work for perceptible directed attacks, because all relevant features are non-robust. We leave a thorough empirical study as interesting future work.

6 Future work

This paper aims to caution the practitioner against blindly following current widespread practices to increase the robust performance of machine learning models. Specifically, adversarial training is currently recognized to be one of the most effective defense mechanisms for ℓ_p -perturbations, significantly outperforming robust performance of standard training. However, we prove that this common wisdom is not applicable for directed attacks – that are perceptible (albeit consistent) but efficiently focus their attack budget to target ground truth class information – in the low-sample size regime. In particular, in such settings adversarial training can in fact yield worse accuracy than standard training.

In terms of follow-up work on directed attacks in the low-sample regime, there are some concrete questions that would be interesting to explore. For example, as discussed in Section 5, it would be useful to test whether some methods to mitigate the standard accuracy vs. robustness trade-off would also relieve the perils of adversarial training for directed attacks. Further, we hypothesize, independent of the attack during test time, it is important in the small sample-size regime to choose perturbation sets during training that align with the ground truth signal (such as rotations for data with inherent rotation). If this hypothesis were to be confirmed, it would break with yet another general rule that the best defense perturbation type should always match the attack during evaluation. The insights from this study might also be helpful in the context of searching for good defense perturbations.

References

- [1] Alayrac, J.-B., Uesato, J., Huang, P.-S., Fawzi, A., Stanforth, R., and Kohli, P. Are labels required for improving adversarial robustness? *Advances in Neural Information Processing Systems*, pp. 12214–12223, 2019.
- [2] Andriushchenko, M. and Flammarion, N. Understanding and improving fast adversarial training. *Advances in Neural Information Processing Systems*, 2020.
- [3] Bai, T., Luo, J., Zhao, J., Wen, B., and Wang, Q. Recent advances in adversarial training for adversarial robustness. In *International Joint Conference on Artificial Intelligence*, pp. 4312–4321, Aug 2021.
- [4] Balaji, Y., Goldstein, T., and Hoffman, J. Instance adaptive adversarial training: Improved accuracy tradeoffs in neural nets. *arXiv preprint arXiv:1910.08051*, 2019.
- [5] Bradski, G. The OpenCV Library. *Dr. Dobb’s Journal of Software Tools*, 2000.
- [6] Carmon, Y., Ragunathan, A., Schmidt, L., Liang, P., and Duchi, J. C. Unlabeled data improves adversarial robustness. In *International Conference on Neural Information Processing Systems*, pp. 11192–11203, Dec 2019.
- [7] Chen, L., Min, Y., Zhang, M., and Karbasi, A. More data can expand the generalization gap between adversarially robust and standard models. In *International Conference on Machine Learning*, pp. 1670–1680, Jun 2020.
- [8] Cheng, M., Lei, Q., Chen, P.-Y., Dhillon, I., and Hsieh, C.-J. CAT: Customized adversarial training for improved robustness. *arXiv preprint arXiv:2002.06789*, 2020.

- [9] Chizat, L. and Bach, F. Implicit bias of gradient descent for wide two-layer neural networks trained with the logistic loss. In *International Conference on Learning Theory*, pp. 1305–1338, Jul 2020.
- [10] Ding, G. W., Sharma, Y., Lui, K. Y. C., and Huang, R. MMA training: Direct input space margin maximization through adversarial training. In *International Conference on Learning Representations*, Apr 2020.
- [11] Dobriban, E., Hassani, H., Hong, D., and Robey, A. Provable tradeoffs in adversarially robust classification. *arXiv preprint arXiv:2006.05161*, 2020.
- [12] Donhauser, K., Tifrea, A., Aerni, M., Heckel, R., and Yang, F. Interpolation can hurt robust generalization even when there is no noise. In *Advances in Neural Information Processing Systems*, Dec 2021.
- [13] Engstrom, L., Tran, B., Tsipras, D., Schmidt, L., and Madry, A. Exploring the landscape of spatial robustness. In *International Conference on Machine Learning*, pp. 1802–1811, Jun 2019.
- [14] Eykholt, K., Evtimov, I., Fernandes, E., Li, B., Rahmati, A., Xiao, C., Prakash, A., Kohno, T., and Song, D. Robust physical-world attacks on deep learning visual classification. In *IEEE Conference on Computer Vision and Pattern Recognition*, pp. 1625–1634, Jun 2018.
- [15] Ghiasi, A., Shafahi, A., and Goldstein, T. Breaking certified defenses: semantic adversarial examples with spoofed robustness certificates. In *International Conference on Learning Representations*, Apr 2019.
- [16] Gilmer, J., Adams, R. P., Goodfellow, I., Andersen, D., and Dahl, G. E. Motivating the rules of the game for adversarial example research. *arXiv preprint arXiv:1807.06732*, 2018.
- [17] Goodfellow, I., Shlens, J., and Szegedy, C. Explaining and harnessing adversarial examples. In *International Conference on Learning Representations*, pp. 1–10, Jan 2015.
- [18] He, K., Zhang, X., Ren, S., and Sun, J. Deep residual learning for image recognition. In *IEEE Conference on Computer Vision and Pattern Recognition*, pp. 770–778, Jun 2016.
- [19] Ilyas, A., Santurkar, S., Tsipras, D., Engstrom, L., Tran, B., and Madry, A. Adversarial examples are not bugs, they are features. In *Advances in Neural Information Processing Systems*, pp. 125–136, Dec 2019.
- [20] Javanmard, A., Soltanolkotabi, M., and Hassani, H. Precise tradeoffs in adversarial training for linear regression. In *Conference on Learning Theory*, pp. 2034–2078, Apr 2020.
- [21] Ji, Z. and Telgarsky, M. The implicit bias of gradient descent on nonseparable data. In *Conference on Learning Theory*, pp. 1772–1798, Jun 2019.
- [22] Khim, J. and Loh, P.-L. Adversarial risk bounds via function transformation. *arXiv preprint arXiv:1810.09519*, 2018.
- [23] Laidlaw, C., Singla, S., and Feizi, S. Perceptual adversarial robustness: Defense against unseen threat models. In *International Conference on Learning Representation*, Jun 2021.
- [24] Lamb, A., Verma, V., Kannala, J., and Bengio, Y. Interpolated adversarial training: Achieving robust neural networks without sacrificing too much accuracy. In *ACM Workshop on Artificial Intelligence and Security*, pp. 95–103, 2019.
- [25] Lee, S., Lee, H., and Yoon, S. Adversarial Vertex Mixup: Toward better adversarially robust generalization. In *IEEE/CVF Conference on Computer Vision and Pattern Recognition*, pp. 272–281, Jun 2020.

- [26] Li, B., Wang, S., Jana, S., and Carin, L. Towards understanding fast adversarial training. *arXiv preprint arXiv:2006.03089*, 2021.
- [27] Lin, W.-A., Lau, C. P., Levine, A., Chellappa, R., and Feizi, S. Dual manifold adversarial robustness: Defense against Lp and non-Lp adversarial attacks. In *Advances in Neural Information Processing Systems*, pp. 3487–3498, Dec 2020.
- [28] Liu, C., Salzmänn, M., Lin, T., Tomioka, R., and Süssstrunk, S. On the loss landscape of adversarial training: Identifying challenges and how to overcome them. In *Advances in Neural Information Processing Systems*, pp. 21476–21487, 2020.
- [29] Luo, B., Liu, Y., Wei, L., and Xu, Q. Towards imperceptible and robust adversarial example attacks against neural networks. In *AAAI Conference on Artificial Intelligence and Innovative Applications*, Feb 2018.
- [30] Madry, A., Makelov, A., Schmidt, L., Tsipras, D., and Vladu, A. Towards deep learning models resistant to adversarial attacks. In *International Conference on Learning Representations*, 2018.
- [31] Mantecón, T., del Blanco, C. R., Jaureguizar, F., and García, N. A real-time gesture recognition system using near-infrared imagery. *PLOS ONE*, pp. 1–17, Oct 2019.
- [32] Moosavi-Dezfooli, S.-M., Fawzi, A., and Frossard, P. Deepfool: a simple and accurate method to fool deep neural networks. In *IEEE conference on computer vision and pattern recognition*, pp. 2574–2582, Jun 2016.
- [33] Mujahid, A., Awan, M. J., Yasin, A., Mohammed, M. A., Damaševičius, R., Maskeliūnas, R., and Abdulkareem, K. H. Real-time hand gesture recognition based on deep learning YOLOv3 model. *Applied Sciences*, 2021.
- [34] Nacson, M. S., Srebro, N., and Soudry, D. Stochastic gradient descent on separable data: Exact convergence with a fixed learning rate. In *The 22th International Conference on Artificial Intelligence and Statistics*, pp. 3051–3059, Apr 2019.
- [35] Nagarajan, V. and Kolter, J. Z. Uniform convergence may be unable to explain generalization in deep learning. In *Advances in Neural Information Processing Systems*, pp. 11611–11622, Dec 2019.
- [36] Oudah, M., Al-Naji, A., and Chahl, J. Hand gesture recognition based on computer vision: A review of techniques. *Journal of Imaging*, 2020.
- [37] Phan, H. [huyvnphan/pytorch_cifar10](https://github.com/huyvnphan/pytorch_cifar10), 1 2021.
- [38] Raghunathan, A., Xie, S. M., Yang, F., Duchi, J., and Liang, P. Understanding and mitigating the tradeoff between robustness and accuracy. In *International Conference on Machine Learning*, pp. 7909–7919, Jul 2020.
- [39] Rice, L., Wong, E., and Kolter, Z. Overfitting in adversarially robust deep learning. In *International Conference on Machine Learning*, pp. 8093–8104, Jul 2020.
- [40] Sagawa*, S., Koh*, P. W., Hashimoto, T. B., and Liang, P. Distributionally robust neural networks. In *International Conference on Learning Representations*, Apr 2020.
- [41] Sanyal, A., Dokania, P. K., Kanade, V., and Torr, P. How benign is benign overfitting? In *International Conference on Learning Representations*, Apr 2020.
- [42] Schmidt, L., Santurkar, S., Tsipras, D., Talwar, K., and Madry, A. Adversarially robust generalization requires more data. In *Advances in Neural Information Processing Systems*, pp. 5019–5031, Dec 2018.

- [43] Schneider, S., Rusak, E., Eck, L., Bringmann, O., Brendel, W., and Bethge, M. Improving robustness against common corruptions by covariate shift adaptation. In Larochelle, H., Ranzato, M., Hadsell, R., Balcan, M. F., and Lin, H. (eds.), *Advances in Neural Information Processing Systems*, pp. 11539–11551, Dec 2020.
- [44] Springer, J. M., Mitchell, M., and Kenyon, G. T. Adversarial perturbations are not so weird: Entanglement of robust and non-robust features in neural network classifiers. *arXiv preprint arXiv:2102.05110*, 2021.
- [45] Stutz, D., Hein, M., and Schiele, B. Disentangling adversarial robustness and generalization. In *IEEE/CVF Conference on Computer Vision and Pattern Recognition*, pp. 6967–6987, Jun 2019.
- [46] Szegedy, C., Zaremba, W., Sutskever, I., Bruna, J., Erhan, D., Goodfellow, I., and Fergus, R. Intriguing properties of neural networks. In *International Conference on Learning Representations*, apr 2014.
- [47] Telgarsky, M. Margins, shrinkage, and boosting. In *International Conference on Machine Learning*, pp. 307–315, Jun 2013.
- [48] Tsipras, D., Santurkar, S., Engstrom, L., Turner, A., and Madry, A. Robustness may be at odds with accuracy. In *International Conference on Learning Representations*, May 2019.
- [49] Vershynin, R. Introduction to the non-asymptotic analysis of random matrices. *arXiv preprint arXiv:1011.3027*, 2010.
- [50] Welinder, P., Branson, S., Mita, T., Wah, C., Schroff, F., Belongie, S., and Perona, P. Caltech-UCSD Birds 200. Technical Report CNS-TR-2010-001, California Institute of Technology, 2010.
- [51] Wong, E., Rice, L., and Kolter, J. Z. Fast is better than free: Revisiting adversarial training. In *International Conference on Learning Representations*, Apr 2020.
- [52] Wu, T., Tong, L., and Vorobeychik, Y. Defending against physically realizable attacks on image classification. In *International Conference on Learning Representations*, Apr 2020.
- [53] Xu, M., Zhang, J., Ni, B., Li, T., Wang, C., Tian, Q., and Zhang, W. Adversarial domain adaptation with domain mixup. In *AAAI Conference on Artificial Intelligence*, pp. 6502–6509, Feb 2020.
- [54] Yang, S., Premaratne, P., and Vial, P. Hand gesture recognition: An overview. In *IEEE International Conference on Broadband Network Multimedia Technology*, pp. 63–69, 2013.
- [55] Yin, D., Kannan, R., and Bartlett, P. Rademacher complexity for adversarially robust generalization. In *International conference on machine learning*, pp. 7085–7094, Jun 2019.
- [56] Zhai, R., Cai, T., He, D., Dan, C., He, K., Hopcroft, J., and Wang, L. Adversarially robust generalization just requires more unlabeled data. *arXiv preprint arXiv:1906.00555*, 2019.
- [57] Zhang, H., Yu, Y., Jiao, J., Xing, E., Ghaoui, L. E., and Jordan, M. Theoretically principled trade-off between robustness and accuracy. In *International Conference on Machine Learning*, pp. 7472–7482, Jun 2019.
- [58] Zhao, Z., Liu, Z., and Larson, M. Towards large yet imperceptible adversarial image perturbations with perceptual color distance. In *IEEE/CVF Conference on Computer Vision and Pattern Recognition*, pp. 1039–1048, 2020.
- [59] Zhou, B., Lapedriza, A., Khosla, A., Oliva, A., and Torralba, A. Places: A 10 million image database for scene recognition. *IEEE Transactions on Pattern Analysis and Machine Intelligence*, 2017.
- [60] Zhou, J., Liang, C., and Chen, J. Manifold projection for adversarial defense on face recognition. In *European Conference on Computer Vision*, pp. 288–305, Aug 2020.

A Theoretical statements for the linear model

Before we present the proof of the theorem, we introduce two lemmas are of separate interest that are used throughout the proof of Theorem 1. Recall that the definition of the (standard normalized) maximum- ℓ_2 -margin solution (max-margin solution in short) of a dataset $D = \{(x_i, y_i)\}_{i=1}^n$ corresponds to

$$\hat{\theta} := \arg \max_{\|\theta\|_2 \leq 1} \min_{i \in [n]} y_i \theta^\top x_i, \quad (10)$$

by simply setting $\epsilon_{\text{tr}} = 0$ in Equation (4). The ℓ_2 -margin of $\hat{\theta}$ then reads $\min_{i \in [n]} y_i \hat{\theta}^\top x_i$. Furthermore for a dataset $D = \{(x_i, y_i)\}_{i=1}^n$ we refer to the induced dataset \tilde{D} as the dataset with covariate vectors stripped of the first element, i.e.

$$\tilde{D} = \{(\tilde{x}_i, y_i)\}_{i=1}^n := \{((x_i)_{[2:d]}, y_i)\}_{i=1}^n, \quad (11)$$

where $(x_i)_{[2:d]}$ refers to the last $d-1$ elements of the vector x_i . Furthermore, remember that for any vector z , $z_{[j]}$ refers to the j -th element of z and e_j denotes the j -th canonical basis vector. Further, recall the distribution \mathbb{P}_r as defined in Section 3.1: the label $y \in \{+1, -1\}$ is drawn with equal probability and the covariate vector is sampled as $x = [y \frac{r}{2}, \tilde{x}]$ where $\tilde{x} \in \mathbb{R}^{d-1}$ is a random vector drawn from a standard normal distribution, i.e. $\tilde{x} \sim \mathcal{N}(0, \sigma^2 I_{d-1})$. We generally allow r , used to sample the training data, to differ from r_{test} , which is used during test time.

The following lemma derives a closed-form expression for the normalized max-margin solution for any dataset with fixed separation r in the signal component, and that is linearly separable in the last $d-1$ coordinates with margin $\tilde{\gamma}$.

Lemma A.1. *Let $D = \{(x_i, y_i)\}_{i=1}^n$ be a dataset that consists of points $(x, y) \in \mathbb{R}^d \times \{\pm 1\}$ and $x_{[1]} = y \frac{r}{2}$, i.e. the covariates x_i are deterministic in their first coordinate given y_i with separation distance r . Furthermore, let the induced dataset \tilde{D} also be linearly separable by the normalized max- ℓ_2 -margin solution $\tilde{\theta}$ with an ℓ_2 -margin $\tilde{\gamma}$. Then, the normalized max-margin solution of the original dataset D is given by*

$$\hat{\theta} = \frac{1}{\sqrt{r^2 + 4\tilde{\gamma}^2}} \left[r, 2\tilde{\gamma}\tilde{\theta} \right]. \quad (12)$$

Further, the standard accuracy of $\hat{\theta}$ for data drawn from $\mathbb{P}_{r_{\text{test}}}$ reads

$$\mathbb{P}_{r_{\text{test}}}(Y\hat{\theta}^\top X > 0) = \Phi\left(\frac{r r_{\text{test}}}{4\sigma \tilde{\gamma}}\right). \quad (13)$$

The proof can be found in Section A.3. The next lemma provides high probability upper and lower bounds for the margin $\tilde{\gamma}$ of \tilde{D} when \tilde{x}_i are drawn from the normal distribution.

Lemma A.2. *Let $\tilde{D} = \{(\tilde{x}_i, y_i)\}_{i=1}^n$ be a random dataset where $y_i \in \{\pm 1\}$ are equally distributed and $\tilde{x}_i \sim \mathcal{N}(0, \sigma I_{d-1})$ for all i , and $\tilde{\gamma}$ is the maximum ℓ_2 margin that can be written as*

$$\tilde{\gamma} = \max_{\|\tilde{\theta}\|_2 \leq 1} \min_{i \in [n]} y_i \tilde{\theta}^\top \tilde{x}_i.$$

Then, for any $t \geq 0$, with probability greater than $1 - 2e^{-\frac{t^2}{2}}$, we have $\tilde{\gamma}_{\min}(t) \leq \tilde{\gamma} \leq \tilde{\gamma}_{\max}(t)$ where

$$\tilde{\gamma}_{\max}(t) = \sigma \left(\sqrt{\frac{d-1}{n}} + 1 + \frac{t}{\sqrt{n}} \right), \quad \tilde{\gamma}_{\min}(t) = \sigma \left(\sqrt{\frac{d-1}{n}} - 1 - \frac{t}{\sqrt{n}} \right).$$

A.1 Proof of Theorem 3.1

Given a dataset $D = \{(x_i, y_i)\}$ drawn from \mathbb{P}_r , it is easy to see that the (normalized) ϵ_{tr} -robust max-margin solution (4) of D with respect to signal-attacking perturbations $T(\epsilon_{\text{tr}}; x_i)$ as defined in Equation (3), can be written as

$$\begin{aligned}\hat{\theta}^{\epsilon_{\text{tr}}} &= \arg \max_{\|\theta\|_2 \leq 1} \min_{i \in [n], x'_i \in T(x_i; \epsilon_{\text{tr}})} y_i \theta^\top x'_i \\ &= \arg \max_{\|\theta\|_2 \leq 1} \min_{i \in [n], |\beta| \leq \epsilon_{\text{tr}}} y_i \theta^\top (x_i + \beta e_1) \\ &= \arg \max_{\|\theta\|_2 \leq 1} \min_{i \in [n]} y_i \theta^\top (x_i - y_i \epsilon_{\text{tr}} \text{sign}(\theta_{[1]}) e_1).\end{aligned}$$

Note that by definition, it is equivalent to the (standard normalized) max-margin solution $\hat{\theta}$ of the shifted dataset $D_{\epsilon_{\text{tr}}} = \{(x_i - y_i \epsilon_{\text{tr}} \text{sign}(\theta_{[1]}) e_1, y_i)\}_{i=1}^n$. Since $D_{\epsilon_{\text{tr}}}$ satisfies the assumptions of Lemma A.1, it then follows directly that the normalized ϵ_{tr} -robust max-margin solution reads

$$\hat{\theta}^{\epsilon_{\text{tr}}} = \frac{1}{\sqrt{(r - 2\epsilon_{\text{tr}})^2 + 4\tilde{\gamma}^2}} \left[r - 2\epsilon_{\text{tr}}, 2\tilde{\gamma}\hat{\theta} \right], \quad (14)$$

by replacing r by $r - 2\epsilon_{\text{tr}}$ in Equation (12). Similar to above, $\tilde{\theta} \in R^{d-1}$ is the (standard normalized) max-margin solution of $\{(\tilde{x}_i, y_i)\}_{i=1}^n$ and $\tilde{\gamma}$ the corresponding margin.

Proof of 1. We can now compute the ϵ_{te} -robust accuracy of the ϵ_{tr} -robust max-margin estimator $\hat{\theta}^{\epsilon_{\text{tr}}}$ for a given dataset D as a function of $\tilde{\gamma}$. Note that in the expression of $\hat{\theta}^{\epsilon_{\text{tr}}}$, all values are fixed for a fixed dataset, while $0 \leq \epsilon_{\text{tr}} \leq r - 2\tilde{\gamma}_{\text{max}}$ can be chosen. First note that for a test distribution \mathbb{P}_r , the ϵ_{te} -robust accuracy, defined as one minus the robust error (Equation (1)), for a classifier associated with a vector θ , can be written as

$$\begin{aligned}\text{Acc}(\theta; \epsilon_{\text{te}}) &= \mathbb{E}_{X, Y \sim \mathbb{P}_r} \left[\mathbb{I} \left\{ \min_{x' \in T(X; \epsilon_{\text{te}})} Y \theta^\top x' > 0 \right\} \right] \\ &= \mathbb{E}_{X, Y \sim \mathbb{P}_r} \left[\mathbb{I} \{ Y \theta^\top X - \epsilon_{\text{te}} \theta_{[1]} > 0 \} \right] = \mathbb{E}_{X, Y \sim \mathbb{P}_r} \left[\mathbb{I} \{ Y \theta^\top (X - Y \epsilon_{\text{te}} \text{sign}(\theta_{[1]}) e_1) > 0 \} \right]\end{aligned} \quad (15)$$

Now, recall that by Equation (14) and the assumption in the theorem, we have $r - 2\epsilon_{\text{tr}} > 0$, so that $\text{sign}(\hat{\theta}^{\epsilon_{\text{tr}}}) = 1$. Further, using the definition of the $T(\epsilon_{\text{tr}}; x)$ in Equation (3) and by definition of the distribution \mathbb{P}_r , we have $X_{[1]} = Y \frac{r}{2}$. Plugging into Equation (15) then yields

$$\begin{aligned}\text{Acc}(\hat{\theta}^{\epsilon_{\text{tr}}}; \epsilon_{\text{te}}) &= \mathbb{E}_{X, Y \sim \mathbb{P}_r} \left[\mathbb{I} \{ Y \hat{\theta}^{\epsilon_{\text{tr}}} \top (X - Y \epsilon_{\text{te}} e_1) > 0 \} \right] \\ &= \mathbb{E}_{X, Y \sim \mathbb{P}_r} \left[\mathbb{I} \{ Y \hat{\theta}^{\epsilon_{\text{tr}}} \top (X_{-1} + Y \left(\frac{r}{2} - \epsilon_{\text{te}} \right) e_1) > 0 \} \right] \\ &= \mathbb{P}_{r-2\epsilon_{\text{te}}} (Y \hat{\theta}^{\epsilon_{\text{tr}}} \top X > 0)\end{aligned}$$

where X_{-1} is a shorthand for the random vector $X_{-1} = (0; X_{[2]}, \dots, X_{[d]})$. The assumptions in Lemma A.1 ($D_{\epsilon_{\text{tr}}}$ is linearly separable) are satisfied whenever the $n < d - 1$ samples are distinct, i.e. with probability one. Hence applying Lemma A.1 with $r_{\text{test}} = r - 2\epsilon_{\text{te}}$ and $r = r - 2\epsilon_{\text{tr}}$ yields

$$\text{Acc}(\hat{\theta}^{\epsilon_{\text{tr}}}; \epsilon_{\text{te}}) = \Phi \left(\frac{r(r - 2\epsilon_{\text{te}})}{4\sigma\tilde{\gamma}} - \epsilon_{\text{tr}} \frac{r - 2\epsilon_{\text{te}}}{2\sigma\tilde{\gamma}} \right). \quad (16)$$

Theorem statement a) then follows by noting that Φ is a monotonically decreasing function in ϵ_{tr} . The expression for the robust error then follows by noting that $1 - \Phi(-z) = \Phi(z)$ for any $z \in \mathbb{R}$ and defining

$$\tilde{\varphi} = \frac{\sigma\tilde{\gamma}}{r/2 - \epsilon_{\text{te}}}. \quad (17)$$

Proof of 2. First define $\varphi_{\min}, \varphi_{\max}$ using $\tilde{\gamma}_{\min}, \tilde{\gamma}_{\max}$ as in Equation (17). Then we have by Equation (16)

$$\begin{aligned} \text{Err}(\hat{\theta}^{\epsilon_{\text{tr}}}; \epsilon_{\text{te}}) - \text{Err}(\hat{\theta}^0; \epsilon_{\text{te}}) &= \text{Acc}(\hat{\theta}^0; \epsilon_{\text{te}}) - \text{Acc}(\hat{\theta}^{\epsilon_{\text{tr}}}; \epsilon_{\text{te}}) \\ &= \Phi\left(\frac{r/2}{\tilde{\varphi}}\right) - \Phi\left(\frac{r/2 - \epsilon_{\text{tr}}}{\tilde{\varphi}}\right) \\ &= \int_{r/2 - \epsilon_{\text{tr}}}^{r/2} \frac{1}{\sqrt{2\pi}\tilde{\varphi}} e^{-\frac{x^2}{\tilde{\varphi}^2}} dx \end{aligned}$$

By plugging in $t = \sqrt{\frac{2\log 2/\delta}{n}}$ in Lemma A.2, we obtain that with probability at least $1 - \delta$ we have

$$\tilde{\gamma}_{\min} := \sigma \left[\sqrt{\frac{d-1}{n}} - \left(1 + \sqrt{\frac{2\log(2/\delta)}{n}}\right) \right] \leq \tilde{\gamma} \leq \sigma \left[\sqrt{\frac{d-1}{n}} + \left(1 + \sqrt{\frac{2\log(2/\delta)}{n}}\right) \right] =: \tilde{\gamma}_{\max}$$

and equivalently $\varphi_{\min} \leq \tilde{\varphi} \leq \varphi_{\max}$.

Now note the general fact that for all $\tilde{\varphi} \leq \sqrt{2}x$ the density function $f(\tilde{\varphi}; x) = \frac{1}{\sqrt{2\pi}\tilde{\varphi}} e^{-\frac{x^2}{\tilde{\varphi}^2}}$ is monotonically increasing in $\tilde{\varphi}$.

By assumption of the theorem, $\tilde{\varphi} \leq \sqrt{2}(r/2 - \epsilon_{\text{tr}})(r/2 - \epsilon_{\text{te}})$ so that $f(\tilde{\varphi}; x) \geq f(\varphi_{\min}; x)$ for all $x \in [r/2 - \epsilon_{\text{tr}}, r/2]$ and therefore

$$\int_{r/2 - \epsilon_{\text{tr}}}^{r/2} \frac{1}{\sqrt{2\pi}\tilde{\varphi}} e^{-\frac{x^2}{\tilde{\varphi}^2}} dx \geq \int_{r/2 - \epsilon_{\text{tr}}}^{r/2} \frac{1}{\sqrt{2\pi}\varphi_{\min}} e^{-\frac{x^2}{\varphi_{\min}^2}} dx = \Phi\left(\frac{r/2}{\varphi_{\min}}\right) - \Phi\left(\frac{r/2 - \epsilon_{\text{tr}}}{\varphi_{\min}}\right).$$

and the statement is proved.

A.2 Proof of Corollary 3.2

We now show that Theorem 3.1 also holds for ℓ_1 -ball perturbations with at most radius ϵ . Following similar steps as in Equation (14), the ϵ_{tr} -robust max-margin solution for ℓ_1 -perturbations can be written as

$$\hat{\theta}^{\epsilon_{\text{tr}}} := \arg \max_{\|\theta\|_2 \leq 1} \min_{i \in [n]} y_i \theta^\top (x_i - y_i \epsilon_{\text{tr}} \text{sign}(\theta_{[j^*(\theta)]}) e_{j^*(\theta)}) \quad (18)$$

where $j^*(\theta) := \arg \max_j |\theta_j|$ is the index of the maximum absolute value of θ . We now prove by contradiction that the robust max-margin solution for this perturbation set (9) is equivalent to the solution (14) for the perturbation set (3). We start by assuming that $\hat{\theta}^{\epsilon_{\text{tr}}}$ does not solve Equation (14), which is equivalent to assuming $1 \notin j^*(\hat{\theta}^{\epsilon_{\text{tr}}})$ by definition. We now show how this assumption leads to a contradiction.

Define the shorthand $j^* := j^*(\hat{\theta}^{\epsilon_{\text{tr}}}) - 1$. Since $\hat{\theta}^{\epsilon_{\text{tr}}}$ is the solution of (18), by definition, we have that $\hat{\theta}^{\epsilon_{\text{tr}}}$ is also the max-margin solution of the shifted dataset $D_{\epsilon_{\text{tr}}} := (x_i - y_i \epsilon_{\text{tr}} \text{sign}(\theta_{[j^*+1]}) e_{j^*+1}, y_i)$. Further, note that by the assumption that $1 \notin j^*(\hat{\theta}^{\epsilon_{\text{tr}}})$, this dataset $D_{\epsilon_{\text{tr}}}$ consists of input vectors $x_i = (y_i \frac{r}{2}, \tilde{x}_i - y_i \epsilon_{\text{tr}} \text{sign}(\theta_{[j^*+1]}) e_{j^*+1})$. Hence via Lemma A.1, $\hat{\theta}^{\epsilon_{\text{tr}}}$ can be written as

$$\hat{\theta}^{\epsilon_{\text{tr}}} = \frac{1}{\sqrt{r^2 - 4(\tilde{\gamma}^{\epsilon_{\text{tr}}})^2}} [r, 2\tilde{\gamma}^{\epsilon_{\text{tr}}} \tilde{\theta}^{\epsilon_{\text{tr}}}], \quad (19)$$

where $\tilde{\theta}^{\epsilon_{\text{tr}}}$ is the normalized max-margin solution of $\tilde{D} := (\tilde{x}_i - y_i \epsilon_{\text{tr}} \text{sign}(\tilde{\theta}_{[j^*]}) e_{j^*}, y_i)$.

We now characterize $\tilde{\theta}^{\epsilon_{\text{tr}}}$. Note that by assumption, $j^* = j^*(\tilde{\theta}^{\epsilon_{\text{tr}}}) = \arg \max_j |\tilde{\theta}_{[j]}^{\epsilon_{\text{tr}}}|$. Hence, the normalized max-margin solution $\tilde{\theta}^{\epsilon_{\text{tr}}}$ is the solution of

$$\tilde{\theta}^{\epsilon_{\text{tr}}} := \arg \max_{\|\tilde{\theta}\|_2 \leq 1} \min_{i \in [n]} y_i \tilde{\theta}^\top \tilde{x}_i - \epsilon_{\text{tr}} |\tilde{\theta}_{[j^*]}| \quad (20)$$

Observe that the minimum margin of this estimator $\tilde{\gamma}^{\epsilon_{\text{tr}}} = \min_{i \in [n]} y_i (\tilde{\theta}^{\epsilon_{\text{tr}}})^\top \tilde{x}_i - \epsilon_{\text{tr}} |\tilde{\theta}_{[j^*]}^{\epsilon_{\text{tr}}}|$ decreases with ϵ_{tr} as the problem becomes harder $\tilde{\gamma}^{\epsilon_{\text{tr}}} \leq \tilde{\gamma}$, where the latter is equivalent to the margin of $\tilde{\theta}^{\epsilon_{\text{tr}}}$ for $\epsilon_{\text{tr}} = 0$. Since $r > 2\tilde{\gamma}_{\max}$ by assumption in the Theorem, by Lemma A.2 with probability at least $1 - 2e^{-\frac{\alpha^2(d-1)}{n}}$, we then have that $r > 2\tilde{\gamma} \geq 2\tilde{\gamma}^{\epsilon_{\text{tr}}}$. Given the closed form of $\tilde{\theta}^{\epsilon_{\text{tr}}}$ in Equation (19), it directly follows that $\tilde{\theta}_{[1]}^{\epsilon_{\text{tr}}} = r > 2\tilde{\gamma}^{\epsilon_{\text{tr}}} \|\tilde{\theta}^{\epsilon_{\text{tr}}}\|_2 = \|\tilde{\theta}_{[2:d]}^{\epsilon_{\text{tr}}}\|_2$ and hence $1 \in j^*(\tilde{\theta}^{\epsilon_{\text{tr}}})$. This contradicts the original assumption $1 \notin j^*(\tilde{\theta}^{\epsilon_{\text{tr}}})$ and hence we established that $\hat{\theta}^{\epsilon_{\text{tr}}}$ for the ℓ_1 -perturbation set (9) has the same closed form (14) as for the perturbation set (3).

The final statement is proved by using the analogous steps as in the proof of 1. and 2. to obtain the closed form of the robust accuracy of $\hat{\theta}^{\epsilon_{\text{tr}}}$.

A.3 Proof of Lemma A.1

We start by proving that $\hat{\theta}$ is of the form

$$\hat{\theta} = [a_1, a_2 \tilde{\theta}] , \quad (21)$$

for $a_1, a_2 > 0$. Denote by $\mathcal{H}(\theta)$ the plane through the origin with normal θ . We define $d((x, y), \mathcal{H}(\theta))$ as the signed euclidean distance from the point $(x, y) \in D \sim \mathbb{P}_r$ to the plane $\mathcal{H}(\theta)$. The signed euclidean distance is defined as the euclidean distance from x to the plane if the point (x, y) is correctly predicted by θ , and the negative euclidean distance from x to the plane otherwise. We rewrite the definition of the max l_2 -margin classifier. It is the classifier induced by the normalized vector $\hat{\theta}$, such that

$$\max_{\theta \in \mathbb{R}^d} \min_{(x, y) \in D} d((x, y), \mathcal{H}(\theta)) = \min_{(x, y) \in D} d((x, y), \mathcal{H}(\hat{\theta})) .$$

We use that D is deterministic in its first coordinate and get

$$\begin{aligned} \max_{\theta} \min_{(x, y) \in D} d((x, y), \mathcal{H}(\theta)) &= \max_{\theta} \min_{(x, y) \in D} y(\theta_{[1]}x_{[1]} + \tilde{\theta}^\top \tilde{x}) \\ &= \max_{\theta} \theta_1 \frac{r}{2} + \min_{(x, y) \in D} y \tilde{\theta}^\top \tilde{x} . \end{aligned}$$

Because $r > 0$, the maximum over all θ has $\hat{\theta}_{[1]} \geq 0$. Take any $a > 0$ such that $\|\tilde{\theta}\|_2 = a$. By definition the max l_2 -margin classifier, $\tilde{\theta}$, maximizes $\min_{(x, y) \in D} d((x, y), \mathcal{H}(\theta))$. Therefore, $\hat{\theta}$ is of the form of Equation (21).

Note that all classifiers induced by vectors of the form of Equation (21) classify D correctly. Next, we aim to find expressions for a_1 and a_2 such that Equation (21) is the normalized max l_2 -margin classifier. The distance from any $x \in D$ to $\mathcal{H}(\hat{\theta})$ is

$$d(x, \mathcal{H}(\hat{\theta})) = |a_1 x_{[1]} + a_2 \tilde{\theta}^\top \tilde{x}| .$$

Using that $x_{[1]} = y \frac{r}{2}$ and that the second term equals $a_2 d(x, \mathcal{H}(\tilde{\theta}))$, we get

$$d(x, \mathcal{H}(\hat{\theta})) = \left| a_1 \frac{r}{2} + a_2 d(x, \mathcal{H}(\tilde{\theta})) \right| = a_1 \frac{r}{2} + \sqrt{1 - a_1^2} d(x, \mathcal{H}(\tilde{\theta})) . \quad (22)$$

Let $(\tilde{x}, y) \in \tilde{D}$ be the point closest in Euclidean distance to $\tilde{\theta}$. This point is also the closest point in Euclidean distance to $\mathcal{H}(\hat{\theta})$, because by Equation (22) $d(x, \mathcal{H}(\hat{\theta}))$ is strictly decreasing for decreasing $d(x, \mathcal{H}(\tilde{\theta}))$. We maximize the minimum margin $d(x, \mathcal{H}(\hat{\theta}))$ with respect to a_1 . Define the vectors $a = [a_1, a_2]$ and $v = \left[\frac{r}{2}, d(x, \mathcal{H}(\tilde{\theta})) \right]$. We find using the dual norm that

$$a = \frac{v}{\|v\|_2}.$$

Plugging the expression of a into Equation (21) yields that $\hat{\theta}$ is given by

$$\hat{\theta} = \frac{1}{\sqrt{r^2 + 4\tilde{\gamma}^2}} [r, 2\tilde{\gamma}\tilde{\theta}].$$

For the second part of the lemma we first decompose

$$\mathbb{P}_{r_{\text{test}}}(Y\hat{\theta}^\top X > 0) = \frac{1}{2}\mathbb{P}_{r_{\text{test}}}\left[\hat{\theta}^\top X > 0 \mid Y = 1\right] + \frac{1}{2}\mathbb{P}_{r_{\text{test}}}\left[\hat{\theta}^\top X < 0 \mid Y = -1\right]$$

We can further write

$$\begin{aligned} \mathbb{P}_{r_{\text{test}}}\left[\hat{\theta}^\top X > 0 \mid Y = 1\right] &= \mathbb{P}_{r_{\text{test}}}\left[\sum_{i=2}^d \hat{\theta}_{[i]} X_{[i]} > -\hat{\theta}_{[1]} X_{[1]} \mid Y = 1\right] \\ &= \mathbb{P}_{r_{\text{test}}}\left[2\tilde{\gamma} \sum_{i=1}^{d-1} \tilde{\theta}_{[i]} X_{[i]} > -r \frac{r_{\text{test}}}{2} \mid Y = 1\right] \\ &= 1 - \Phi\left(-\frac{r r_{\text{test}}}{4\sigma\tilde{\gamma}}\right) = \Phi\left(\frac{r r_{\text{test}}}{4\sigma\tilde{\gamma}}\right) \end{aligned} \quad (23)$$

where Φ is the cumulative distribution function. The second equality follows by multiplying by the normalization constant on both sides and the third equality is due to the fact that $\sum_{i=1}^{d-1} \tilde{\theta}_{[i]} X_{[i]}$ is a zero-mean Gaussian with variance $\sigma^2 \|\tilde{\theta}\|_2^2 = \sigma^2$ since $\tilde{\theta}$ is normalized. Correspondingly we can write

$$\mathbb{P}_{r_{\text{test}}}\left[\hat{\theta}^\top X < 0 \mid Y = -1\right] = \mathbb{P}_{r_{\text{test}}}\left[2\tilde{\gamma} \sum_{i=1}^{d-1} \tilde{\theta}_{[i]} X_{[i]} < -r \left(-\frac{r_{\text{test}}}{2}\right) \mid Y = -1\right] = \Phi\left(\frac{r r_{\text{test}}}{4\sigma\tilde{\gamma}}\right) \quad (24)$$

so that we can combine (23) and (23) and (24) to obtain $\mathbb{P}_{r_{\text{test}}}(Y\hat{\theta}^\top X > 0) = \Phi\left(\frac{r r_{\text{test}}}{4\sigma\tilde{\gamma}}\right)$. This concludes the proof of the lemma.

A.4 Proof of Lemma A.2

The proof plan is as follows. We start from the definition of the max ℓ_2 -margin of a dataset. Then, we rewrite the max ℓ_2 -margin as an expression that includes a random matrix with independent standard normal entries. This allows us to prove the upper and lower bounds for the max- ℓ_2 -margin in Sections A.4.1 and A.4.2 respectively, using non-asymptotic estimates on the singular values of Gaussian random matrices.

Given the dataset $\tilde{D} = \{(\tilde{x}_i, y_i)\}_{i=1}^n$, we define the random matrix

$$X = \begin{pmatrix} \tilde{x}_1^\top \\ \tilde{x}_2^\top \\ \dots \\ \tilde{x}_n^\top \end{pmatrix}. \quad (25)$$

where $\tilde{x}_i \sim \mathcal{N}(0, \sigma I_{d-1})$. Let \mathcal{V} be the class of all perfect predictors of \tilde{D} . For a matrix A and vector b we also denote by $|Ab|$ the vector whose entries correspond to the absolute values of the entries of Ab . Then, by definition

$$\tilde{\gamma} = \max_{v \in \mathcal{V}, \|v\|_2=1} \min_{j \in [n]} |Xv|_{[j]} = \max_{v \in \mathcal{V}, \|v\|_2=1} \min_{j \in [n]} \sigma |Qv|_{[j]}, \quad (26)$$

where $Q = \frac{1}{\sigma}X$ is the scaled data matrix.

In the sequel we will use the operator norm of a matrix $A \in \mathbb{R}^{n \times d-1}$.

$$\|A\|_2 = \sup_{v \in \mathbb{R}^{d-1}, \|v\|_2=1} \|Av\|_2$$

and denote the maximum singular value of a matrix A as $s_{\max}(A)$ and the minimum singular value as $s_{\min}(A)$.

A.4.1 Upper bound

Given the maximality of the operator norm and since the minimum entry of the vector $|Qv|$ must be smaller than $\frac{\|Q\|_2}{\sqrt{n}}$, we can upper bound $\tilde{\gamma}$ by

$$\tilde{\gamma} \leq \sigma \frac{1}{\sqrt{n}} \|Q\|_2.$$

Taking the expectation on both sides with respect to the draw of \tilde{D} and noting $\|Q\|_2 \leq s_{\max}(Q)$, it follows from Corollary 5.35 of [49] that for all $t \geq 0$:

$$\mathbb{P} \left[\sqrt{d-1} + \sqrt{n} + t \geq s_{\max}(Q) \right] \geq 1 - 2e^{-\frac{t^2}{2}}.$$

Therefore, with a probability greater than $1 - 2e^{-\frac{t^2}{2}}$,

$$\tilde{\gamma} \leq \sigma \left(1 + \frac{t + \sqrt{d-1}}{\sqrt{n}} \right).$$

A.4.2 Lower bound

By the definition in Equation (26), if we find a vector $v \in \mathcal{V}$ with $\|v\|_2 = 1$ such that for an $a > 0$, it holds that $\min_{j \in [n]} \sigma |Xv|_{[j]} > a$, then $\tilde{\gamma} > a$.

Recall the definition of the max- ℓ_2 -margin as in Equation 25. As $n < d-1$, the random matrix Q is a wide matrix, i.e. there are more columns than rows and therefore the minimal singular value is 0. Furthermore, Q has rank n almost surely and hence for all $c > 0$, there exists a $v \in \mathbb{R}^{d-1}$ such that

$$\sigma Qv = \mathbf{1}_{\{n\}} c > 0, \quad (27)$$

where $\mathbf{1}_{\{n\}}$ denotes the all ones vector of dimension n . The smallest non-zero singular value of Q , $s_{\min, \text{nonzero}}(Q)$, equals the smallest non-zero singular value of its transpose Q^\top . Therefore, there also exists a $v \in \mathcal{V}$ with $\|v\|_2 = 1$ such that

$$\tilde{\gamma} \geq \min_{j \in [n]} \sigma |Qv|_{[j]} \geq \sigma s_{\min, \text{nonzeros}}(Q^\top) \frac{1}{\sqrt{n}}, \quad (28)$$

where we used the fact that any vector v in the span of non-zero eigenvectors satisfies $\|Qv\|_2 \geq s_{\min, \text{nonzeros}}(Q)$ and the existence of a solution v for any right-hand side as in Equation 27. Taking the expectation on both sides, Corollary 5.35 of [49] yields that with a probability greater than $1 - 2e^{-\frac{t^2}{2}}$, $t \geq 0$ we have

$$\tilde{\gamma} \geq \sigma \left(\frac{\sqrt{d-1} - t}{\sqrt{n}} - 1 \right). \quad (29)$$

B Bounds on the susceptibility score

In Theorem 3.1, we give non-asymptotic bounds on the robust and standard error of a linear classifier trained with adversarial logistic regression. Moreover, we use the robust error decomposition in susceptibility and standard error to gain intuition about how adversarial training may hurt robust generalization. In this section, we complete the result of Theorem 3.1 by also deriving non-asymptotic bounds on the susceptibility score of the max ℓ_2 -margin classifier.

Using the results in Appendix A, we can prove following Corollary B.1, which gives non asymptotic bounds on the susceptibility score.

Corollary B.1. *Assume $d - 1 > n$. For the ϵ_{te} -susceptibility on test samples from \mathbb{P}_r with $2\epsilon_{te} < r$ and perturbation sets in Equation (3) and (9) the following holds:*

For $\epsilon_{tr} < \frac{r}{2} - \tilde{\gamma}_{\max}$, with probability at least $1 - 2e^{-\frac{\alpha^2(d-1)}{2}}$ for any $0 < \alpha < 1$, over the draw of a dataset D with n samples from \mathbb{P}_r , the ϵ_{te} -susceptibility is upper and lower bounded by

$$\begin{aligned} \text{Susc}(\hat{\theta}^{\epsilon_{tr}}; \epsilon_{te}) &\leq \Phi\left(\frac{(r - 2\epsilon_{tr})(\epsilon_{te} - \frac{r}{2})}{2\tilde{\gamma}_{\max}\sigma}\right) - \Phi\left(\frac{(r - 2\epsilon_{tr})(-\epsilon_{te} - \frac{r}{2})}{2\tilde{\gamma}_{\min}\sigma}\right) \\ \text{Susc}(\hat{\theta}^{\epsilon_{tr}}; \epsilon_{te}) &\geq \Phi\left(\frac{(r - 2\epsilon_{tr})(\epsilon_{te} - \frac{r}{2})}{2\tilde{\gamma}_{\min}\sigma}\right) - \Phi\left(\frac{(r - 2\epsilon_{tr})(-\epsilon_{te} - \frac{r}{2})}{2\tilde{\gamma}_{\max}\sigma}\right) \end{aligned} \quad (30)$$

We give the proof in Subsection B.1. Observe that the bounds on the susceptibility score in Corollary B.1 consist of two terms each, where the second term decreases with ϵ_{tr} , but the first term increases. We recognise following two regimes: the max ℓ_2 -margin classifier is close to the ground truth e_1 or not. Clearly, the ground truth classifier has zero susceptibility and hence classifiers close to the ground truth also have low susceptibility. On the other hand, if the max ℓ_2 -margin classifier is not close to the ground truth, then putting less weight on the first coordinate increases invariance to the perturbations along the first direction. Recall that by Lemma A.1, increasing ϵ_{tr} , decreases the weight on the first coordinate of the max ℓ_2 -margin classifier. Furthermore, in the low sample size regime, we are likely not close to the ground truth. Therefore, the regime where the susceptibility decreases with increasing ϵ_{tr} dominates in the low sample size regime.

To confirm the result of Corollary B.1, we plot the mean and standard deviation of the susceptibility score of 5 independent experiments. The results are depicted in Figure 7. We see that for low standard error, when the classifier is reasonably close to the optimal classifier, the susceptibility increases slightly with increasing adversarial budget. However, increasing the adversarial training budget, ϵ_{tr} , further, causes the susceptibility score to drop greatly. Hence, we can recognize both regimes and validate that, indeed, the second regime dominates in the low sample size setting.

B.1 Proof of Corollary B.1

We proof the statement by bounding the robustness of a linear classifier. Recall that the robustness of a classifier is the probability that a classifier does not change its prediction under an adversarial attack. The susceptibility score is then given by

$$\text{Susc}(\hat{\theta}^{\epsilon_{tr}}; \epsilon_{te}) = 1 - \text{Rob}(\hat{\theta}^{\epsilon_{tr}}; \epsilon_{te}). \quad (31)$$

The proof idea is as follows: since the perturbations are along the first basis direction, e_1 , we compute the distance from the robust ℓ_2 -max margin $\hat{\theta}^{\epsilon_{tr}}$ to a point $(X, Y) \sim \mathbb{P}$. Then, we note that the robustness of $\hat{\theta}^{\epsilon_{tr}}$ is given by the probability that the distance along e_1 , from X to the decision plane induced by $\hat{\theta}^{\epsilon_{tr}}$ is greater than ϵ_{te} . Lastly, we use the non-asymptotic bounds of Lemma A.2.

Recall, by Lemma A.1, the max l_2 -margin classifier is of the form of

$$\widehat{\theta}^{\epsilon_{tr}} = \frac{1}{\sqrt{(r - 2\epsilon_{tr})^2 + 4\tilde{\gamma}^2}} \left[r - 2\epsilon_{tr}, 2\tilde{\gamma}\tilde{\theta} \right]. \quad (32)$$

Let $(X, Y) \sim \mathbb{P}$. The distance along e_1 from X to the decision plane induced by $\widehat{\theta}^{\epsilon_{tr}}$, $\mathcal{H}(\widehat{\theta}^{\epsilon_{tr}})$, is given by

$$d_{e_1}(X, \mathcal{H}(\widehat{\theta}^{\epsilon_{tr}})) = \left| X_{[1]} + \frac{1}{\widehat{\theta}_{[0]}^{\epsilon_{tr}}} \sum_{i=2}^d \widehat{\theta}_{[i]}^{\epsilon_{tr}} X_{[i]} \right|.$$

Substituting the expression of $\widehat{\theta}^{\epsilon_{tr}}$ in Equation 32 yields

$$d_{e_1}(X, \mathcal{H}(\widehat{\theta}^{\epsilon_{tr}})) = \left| X_{[1]} + 2\tilde{\gamma} \frac{1}{(r - \epsilon_{tr})} \sum_{i=2}^d \tilde{\theta}_{[i]} X_{[i]} \right|.$$

Let N be a standard normal distributed random variable. By definition $\|\tilde{\theta}\|_2^2 = 1$ and using that a sum of Gaussian random variables is again a Gaussian random variable, we can write

$$d_{e_1}(X, \mathcal{H}(\widehat{\theta}^{\epsilon_{tr}})) = \left| X_{[1]} + 2\tilde{\gamma} \frac{\sigma}{(r - \epsilon_{tr})} N \right|.$$

The robustness of $\widehat{\theta}^{\epsilon_{tr}}$ is given by the probability that $d_{e_1}(X, \mathcal{H}(\widehat{\theta}^{\epsilon_{tr}})) > \epsilon_{te}$. Hence, using that $X_1 = \pm \frac{r}{2}$ with probability $\frac{1}{2}$, we get

$$\text{Rob}(\widehat{\theta}^{\epsilon_{tr}}; \epsilon_{te}) = P \left[\frac{r}{2} + 2\tilde{\gamma} \frac{\sigma}{(r - 2\epsilon_{tr})} N > \epsilon_{te} \right] + P \left[\frac{r}{2} + 2\tilde{\gamma} \frac{\sigma}{(r - \epsilon_{tr})} N < -\epsilon_{te} \right]. \quad (33)$$

We can rewrite Equation 33 in the form

$$\text{Rob}(\widehat{\theta}^{\epsilon_{tr}}; \epsilon_{te}) = P \left[N > \frac{(r - 2\epsilon_{tr})(\epsilon_{te} - \frac{r}{2})}{2\tilde{\gamma}\sigma} \right] + P \left[N < \frac{(r - 2\epsilon_{tr})(-\epsilon_{te} - \frac{r}{2})}{2\tilde{\gamma}\sigma} \right].$$

Recall, that N is a standard normal distributed random variable and denote by Φ the cumulative standard normal density. By definition of the cumulative density function, we find that

$$\text{Rob}(\widehat{\theta}^{\epsilon_{tr}}; \epsilon_{te}) = 1 - \Phi \left(\frac{(r - 2\epsilon_{tr})(\epsilon_{te} - \frac{r}{2})}{2\tilde{\gamma}\sigma} \right) + \Phi \left(\frac{(r - 2\epsilon_{tr})(-\epsilon_{te} - \frac{r}{2})}{2\tilde{\gamma}\sigma} \right).$$

Substituting the bounds on $\tilde{\gamma}$ of Lemma A.2 gives us the non-asymptotic bounds on the robustness score and by Equation 31 also on the susceptibility score.

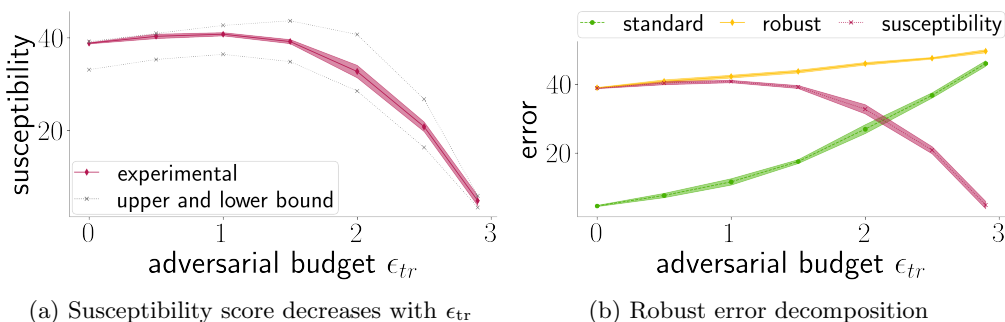


Figure 7: We set $r = 6$, $d = 1000$, $n = 50$ and $\epsilon_{te} = 2.5$. (a) We plot the average susceptibility score and the standard deviation over 5 independent experiments. Note how the bounds closely predict the susceptibility score. (b) For comparison, we also plot the robust error decomposition in susceptibility and standard error. Even though the susceptibility decreases, the robust error increases with increasing adversarial budget ϵ_{tr} .

C Experimental details on the linear model

In this section, we provide detailed experimental details to Figures 3 and 4.

We implement adversarial logistic regression using stochastic gradient descent with a learning rate of 0.01. Note that logistic regression converges logarithmically to the robust max l_2 -margin solution. As a consequence of the slow convergence, we train for up to 10^7 epochs. Both during training and test time we solve $\max_{x'_i \in T(x_i; \epsilon_{tr})} L(f_\theta(x'_i) y_i)$ exactly. Hence, we exactly measure the robust error. Unless specified otherwise, we set $\sigma = 1$, $r = 12$ and $\epsilon_{te} = 4$.

Experimental details on Figure 3 (a) We draw 5 datasets with $n = 50$ samples and input dimension $d = 1000$ from the distribution \mathbb{P} . We then run adversarial logistic regression on all 5 datasets with adversarial training budgets, $\epsilon_{tr} = 1$ to 5. To compute the resulting robust error gap of all the obtained classifiers, we use a test set of size 10^6 . Lastly, we compute the lower bound given in part 2. of Theorem 3.1. (b) We draw 5 datasets with different sizes n between 50 and 10^4 . We take an input dimension of $d = 10^4$ and plot the mean and standard deviation of the robust error after adversarial and standard logistic regression over the 5 samples. (c) We again draw 5 datasets for each d/n constellation and compute the robust error gap for each dataset.

Experimental details on Figure 4 For both (a) and (b) we set $d = 1000$, $\epsilon_{te} = 4$, and vary the adversarial training budget (ϵ_{tr}) from 1 to 5. For every constellation of n and ϵ_{tr} , we draw 10 datasets and show the average and standard deviation of the resulting robust errors. In (b), we set $n = 50$.

D Experimental details on the Waterbirds dataset

In this section, we discuss the experimental details and construction of the Waterbirds dataset in more detail. We also provide ablation studies of attack parameters such as the size of the motion blur kernel, plots of the robust error decomposition with increasing n , and some experiments using early stopping.

The waterbirds dataset To build the Waterbirds dataset, we use the CUB-200 dataset [50], which contains images and labels of 200 bird species, and 4 background classes (forest, jungle/bamboo, water ocean, water lake natural) of the Places dataset [59]. The aim is to recognize whether or not the bird, in a given image, is a waterbird (e.g. an albatros) or a landbird (e.g. a woodpecker). To create the dataset, we randomly sample equally many water- as landbirds from the CUB-200 dataset. Thereafter, we sample for each bird image a random background image. Then, we use the segmentation provided in the CUB-200 dataset to segment the birds from their original images and paste them onto the randomly sampled backgrounds. The resulting images have a size of 256×256 . Moreover, we also resize the segmentations such that we have the correct segmentation profiles of the birds in the new dataset as well. For the concrete implementation, we use the code provided by [40].

Experimental training details Following the example of [40], we use a ResNet50 pretrained on the ImageNet dataset for all experiments, a weight-decay of 10^{-4} , and train for 300 epochs using the Adam optimizer. Extensive fine-tuning of the learning rate resulted in an optimal learning rate of 0.006 for all experiments in the low sample size regime. Adversarial training is implemented as suggested in [30]: at each iteration we find the worst case perturbation with an exact or approximate method. In all our experiments, the resulting classifier interpolates the training set. We plot the mean over all runs and the standard deviation of the mean.

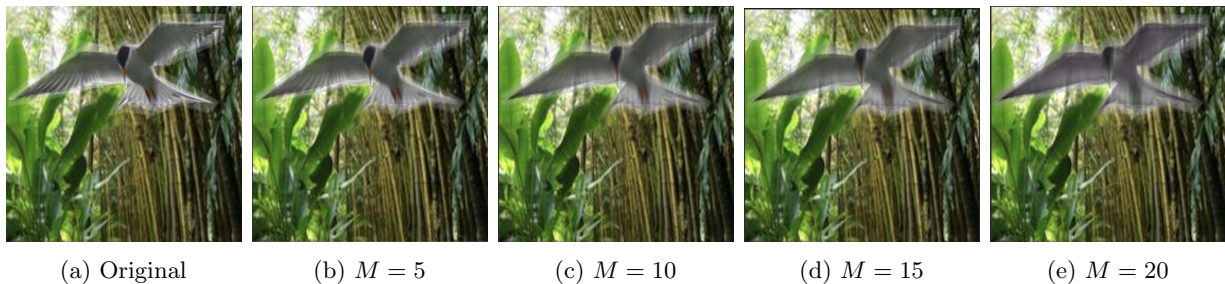


Figure 8: We perform an ablation study of the motion blur kernel size, which corresponds to the severity level of the blur. We see that for increasing M , the severity of the motion blur increases. In particular, note that for $M = 15$ and even $M = 20$, the bird remains recognizable; we do not semantically change the class, i.e. the perturbations are consistent.

Specifics to the motion blur attack Fast moving objects or animals are hard to photograph due to motion blur. Hence, when trying to classify or detect moving objects from images, it is imperative that the classifier is robust against reasonable levels of motion blur. We implement the attack as follows. First, we segment the bird from the original image, then use a blur filter and lastly, we paste the blurred bird back onto the background. We are able to apply more severe blur, by enlarging the kernel of the filter. See Figure 8 for an ablation study of the kernel size.

The motion blur filter is implemented as follows. We use a kernel of size $M \times M$ and build the filter as follows: we fill the row $(M - 1)/2$ of the kernel with the value $1/M$. Thereafter, we use the 2D convolution implementation of OpenCV (`filter2D`) [5] to convolute the kernel with the image. Note that applying a rotation before the convolution to the kernel, changes the direction of the resulting motion blur. Lastly, we find the most detrimental level of motion blur using a list-search over all levels up to M_{max} .

Specifics to the adversarial illumination attack An adversary can hide objects using poor lightning conditions, which can for example arise from shadows or bright spots. To model poor lighting conditions on the object only (or targeted to the object), we use the adversarial illumination attack. The attack is constructed as follows: First, we segment the bird from their background. Then we apply an additive constant ϵ to the bird, where the absolute size of the constant satisfies $|\epsilon| < \epsilon_{te} = 0.3$. Thereafter, we clip the values of the bird images to $[0, 1]$, and lastly, we paste the bird back onto the background. See Figure 9 for an ablation of the parameter ϵ of the attack. It is non-trivial how to (approximately) find the worst perturbation. We find an approximate solution by searching over all perturbations with increments of size ϵ_{te}/K_{max} . Denote by

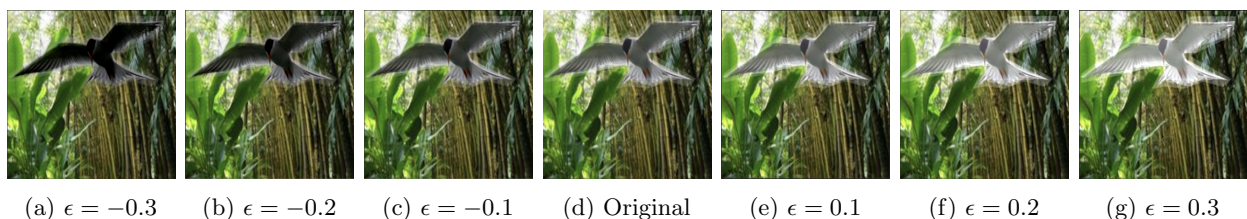


Figure 9: We perform an ablation study of the different lighting changes of the adversarial illumination attack. Even though the directed attack attacks the signal component in the image, the bird remains recognizable in all cases.

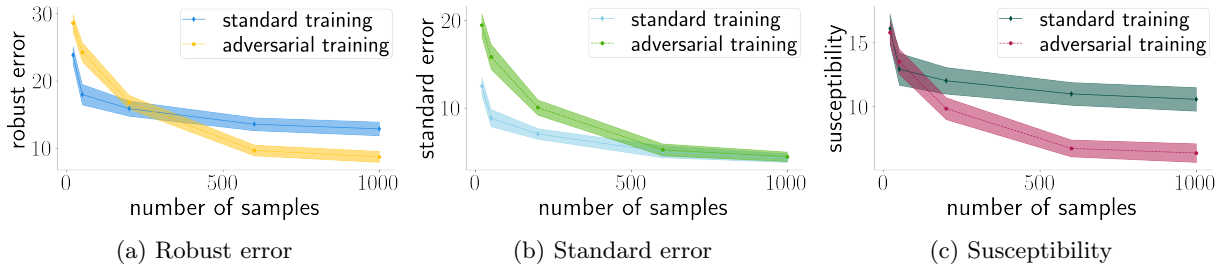


Figure 10: We plot the robust error decomposition of the experiments depicted in Figure 5c. The plots depict the mean and standard deviation of the mean over several independent experiments. We see that, in comparison to standard training, the reduction in susceptibility for adversarial training is minimal in the low sample size regime. Moreover, the increase in standard error of adversarial training is quite severe, leading to an overall increase in robust error in the low sample size regime.

seg, the segmentation profile of the image x . We consider all perturbed images in the form of

$$x_{pert} = (1 - seg)x + seg(x + \epsilon \frac{K}{K_{max}} 1_{255 \times 255}), \quad K \in [-K_{max}, K_{max}].$$

During training time we set $K_{max} = 16$ and therefore search over 33 possible images. During test time we search over 65 images ($K_{max} = 32$).

Early stopping In all our experiments on the Waterbirds dataset, a parameter search lead to an optimal weight-decay and learning rate of 10^{-4} and 0.006 respectively. Another common regularization technique is early stopping, where one stops training on the epoch where the classifier achieves minimal robust error on a hold-out dataset. To understand if early stopping can mitigate the effect of adversarial training aggregating robust generalization in comparison to standard training, we perform the following experiment. On the Waterbirds dataset of size $n = 20$ and considering the adversarial illumination attack, we compare standard training with early stopping and adversarial training ($\epsilon_{tr} = \epsilon_{te} = 0.3$) with early stopping. Considering several independent experiments, early stopped adversarial training has an average robust error of 33.5 a early stopped standard training 29.1. Hence, early stopping does decrease the robust error gap, but does not close it.

Error decomposition with increasing n In Figure 5c, we see that adversarial training hurts robust generalization in the small sample size regime. For completeness, we plot the robust error composition for adversarial and standard training in Figure 10. We see that in the low sample size regime, the drop in susceptibility that adversarial training achieves in comparison to standard training, is much lower than the increase in standard error. Conversely, in the high sample regime, the drop of susceptibility from adversarial training over standard training is much bigger than the increase in standard error.

E Experimental details on CIFAR10

In this section, we give the experimental details on the CIFAR10-based experiments shown in Figures 1 and 12. Moreover, we also conduct similar experiments using different neural network architectures. First, we give the full experimental details and then provide the results of the experiments using the different architectures.

Subsampling CIFAR10 In all our experiments we subsample CIFAR10 to simulate the low sample size regime. We ensure that for all subsampled versions the number of samples of each class are equal. Hence, if we subsample to 500 training images, then each class has exactly 50 images, which are drawn uniformly from the $5k$ training images of the respective class.

Mask perturbation on CIFAR10 We consider square black-mask perturbations; the attacker can set in the image a patch of size 2×2 to zero. The attack is a simplification of the patch-attack as considered in [52]. We show an example of a black-mask attack on each of the classes in CIFAR10 in Figure 11. Clearly, the mask reduces the information about the class in the image as it occludes part of the object in the image.



Figure 11: We show an example of a mask perturbation for all 10 classes of CIFAR10. Even though the attack occludes part of the images, a human can still easily classify all images correctly.

During test time, we evaluate the attack exactly by means of a full grid search over all possible windows. Note that a full grid search requires 900 forward passes to evaluate one image, which is computationally too expensive during training time. Therefore, we use the same approximation as in [52] at training time. For each image in the training batch, we compute the gradient from the loss with respect to the input. Using that gradient, which is a tensor in $\mathbb{R}^{3 \times 32 \times 32}$, we compute the l_1 -norm of each patch by a full grid search and save the upper left coordinates of the K windows with largest l_1 -norm. The intuition is that windows with high l_1 -norm are more likely to change the prediction. Out of the K identified candidate windows, we take the most loss worsening by means of a full list-search.

Experimental training details For all our experiments on CIFAR10, we adjusted the code provided by [37]. As typically done for CIFAR10, we augment the data with random cropping and horizontal flipping. For the experiments with results depicted in Figures 1 and 12, we use a ResNet18 network and train for 100 epochs. We tune the parameters learning rate and weight decay for low robust error. For standard training, we use a learning rate of 0.01 with equal weight decay. For adversarial training, we use a learning rate of 0.015 and a weight decay of 10^{-4} . We run each experiment three times for every dataset with different initialization seeds, and plot the average and standard deviation over the runs.

For the experiments in Figure 1 and 13 we use an attack strength of $K = 4$. Recall that we perform a full grid search at test time and hence have a good approximation of the robust accuracy and susceptibility score.

Increasing training attack strength We investigate the influence of the attack strength K on the robust error for adversarial training. We take $\epsilon_{\text{tr}} = 2$ and $n = 500$ and vary K . The results are depicted in Figure 12. We see that for increasing K , the susceptibility decreases, but the standard error increases more severely, resulting in an increasing robust error.

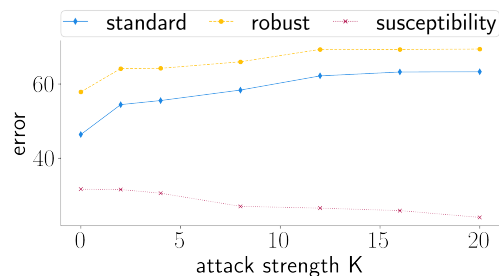


Figure 12: We plot the standard error, robust error and susceptibility for varying attack strengths K . We see that the larger K , the lower the susceptibility, but the higher the standard error.

Robust error decomposition In Figure 1, we see that the robust error increases for adversarial training compared to standard training in the low sample size regime, but the opposite holds when enough samples are available. For completeness, we provide a full decomposition of the robust error in standard error and susceptibility for standard and adversarial training. We plot the decomposition in Figure 13.

Multiple networks on CIFAR10 We run adversarial training for multiple network architectures on subsampled CIFAR10 ($n = 500$) with mask perturbations of size 2×2 and an attack strength of $K = 4$. We plot the results in Table 1. For all the different architectures, we notice a similar increase in robust error when trained with adversarial training instead of standard training.

Table 1: We subsample CIFAR10 to a dataset of sample size 500 and perform both standard training (ST) and adversarial training (AT) using different networks. We evaluate the resulting susceptibility score and the robust and standard error.

Adversarial training on CIFAR10						
Architecture	learning rate	weight decay	Train type	standard error	robust error	Susceptibility
ResNet34	0.02	0.025	ST	44	64	50
ResNet34	0.015	10^{-4}	AT	52	66	40
ResNet50	0.015	0.03	ST	45	62	47
ResNet50	0.015	10^{-4}	AT	53	68	45
VGG11bn	0.03	0.01	ST	40	55	43
VGG11bn	0.015	10^{-4}	AT	48	63	34
VGG16bn	0.02	0.01	ST	41	60	48
VGG16bn	0.015	10^{-4}	AT	50	65	42

F Static hand gesture recognition

The goal of static hand gesture or posture recognition is to recognize hand gestures such as a pointing index finger or the okay-sign based on static data such as images [36, 54]. The current use of hand gesture recognition is primarily in the interaction between computers and humans [36]. More specifically, typical practical applications can be found in the environment of games, assisted living, and virtual reality [33]. In the following, we conduct experiments on a hand gesture recognition dataset constructed by [31], which consists of near-infrared stereo images obtained using the Leap Motion device. First, we crop or segment the

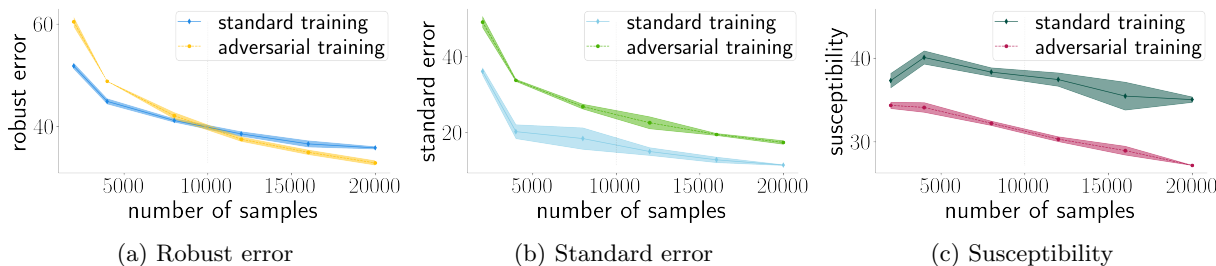


Figure 13: We plot the standard error, robust error and susceptibility of the subsampled datasets of CIFAR10 after adversarial and standard training. For small sample size, adversarial training has higher robust error than standard training. We see that the increase in standard error in comparison to the drop in susceptibility of standard versus robust training, switches between the low and high sample size regimes.



Figure 14: We plot two images, where both correspond to the two different classes. We recognize the "L"-sign in Figure 14a and the index sign in Figure 14b. Observe that the near-infrared images highlight the hand pose well and blends out much of the non-useful or noisy background.

images after which we use logistic regression for classification. We see that adversarial logistic regression deteriorates robust generalization with increasing ϵ_{tr} .

Static hand-gesture dataset We use the dataset made available by [31]. This dataset consists of near-infrared stereo images taken with the Leap Motion device and provides detailed skeleton data. We base our analysis on the images only. The size of the images is 640×240 pixels. The dataset consists of 16 classes of hand poses taken by 25 different people. We note that the variety between the different people is relatively wide; there are men and women with different posture and hand sizes. However, the different samples taken by the same person are alike.

We consider binary classification between the index-pose and L-pose, and take as a training set 30 images of the users 16 to 25. This results in a training dataset of 300 samples. We show two examples of the training dataset in Figure 14, each corresponding to a different class. Observe that the near-infrared images darken the background and successfully highlight the hand-pose. As a test dataset, we take 10 images of each of the two classes from the users 1 to 10 resulting in a test dataset of size 200.

Cropping the dataset To speed up training and ease the classification problem, we crop the images from a size of 640×240 to a size of 200×200 . We crop the images using a basic image segmentation technique to stay as close as possible to real-world applications. The aim is to crop the images such that the hand gesture is centered within the cropped image.

For every user in the training set, we crop an image of the L-pose and the index pose by hand. We call these images the training masks $\{\text{masks}_i\}_{i=1}^{20}$. We note that the more a particular window of an image resembles a mask, the more likely that the window captures the hand gesture correctly. Moreover, the near-infrared images are such that the hands of a person are brighter than the surroundings of the person itself. Based on these two observations, we define the best segment or window, defined by the upper left coordinates (i, j) , for an image x as the solution to the following optimization problem:

$$\arg \min_{i \in [440], j \in [40]} \sum_{l=1}^{20} \|\text{masks}_l - x_{\{i:i+200, j:j+200\}}\|_2^2 - \frac{1}{2} \|x_{\{i+w, j+h\}}\|_1. \quad (34)$$

Equation 34 is solved using a full grid search. We use the result to crop both training and test images. Upon manual inspection of the cropped images, close to all images were perfectly cropped. We replace the handful poorly cropped training images with hand-cropped counterparts.

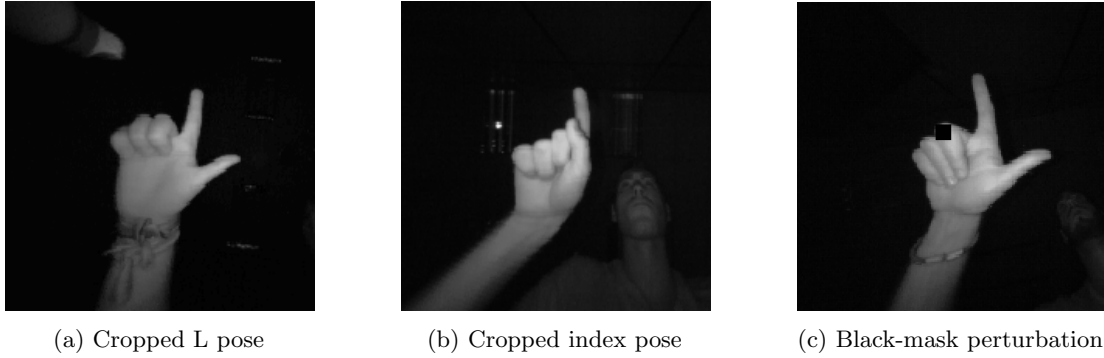


Figure 15: In Figure 15a and 15b we show an example of the images cropped using Equation 34. We see that the hands are centered and the images have a size of 200×200 . In Figure 15c we show an example of the square black-mask perturbation.

Square-mask perturbations Since we use logistic regression, we perform a full grid search to find the best adversarial perturbation at training and test time. For completeness, the upper left coordinates of the optimal black-mask perturbation of size $\epsilon_{tr} \times \epsilon_{tr}$ can be found as the solution to

$$\arg \max_{i \in [200 - \epsilon_{tr}], j \in [200 - \epsilon_{tr}]} \sum_{l, m \in [\epsilon_{tr}]} \theta_{[i:i+l, j:j+m]}. \quad (35)$$

The algorithm is rather slow as we iterate over all possible windows. We show a black-mask perturbation on an L -pose image in Figure 15c.

Results We run adversarial logistic regression with square-mask perturbations on the cropped dataset and vary the adversarial training budget and plot the result in Figure 16. We observe attack that adversarial logistic regression deteriorates robust generalization.

Because we use adversarial logistic regression, we are able to visualize the classifier. Given the classifier induced by θ , we can visualize how it classifies the images by plotting $\frac{\theta - \min_{i \in [d]} \theta_{[i]}}{\max_{i \in [d]} \theta_{[i]}} \in [0, 1]^d$. Recall that the class-prediction of our predictor for a data point (x, y) is given by $\text{sign}(\theta^\top x) \in \{\pm 1\}$. The lighter parts of the resulting image correspond to the class with label 1 and the darker patches with the class corresponding to label -1 .

We plot the classifiers obtained by standard logistic regression and adversarial logistic regression with training adversarial budgets ϵ_{tr} of 10 and 25 in Figure 17. The darker parts in the classifier correspond to patches that are typically bright for the L -pose. Complementary, the lighter patches in the classifier correspond to patches that are typically bright for the index pose. We see that in the case of adversarial logistic regression, the background noise is much higher than for standard logistic regression. In other words, adversarial logistic regression puts more weight on non-signal parts in the images to classify the training dataset and hence exhibits worse performance on the test dataset.

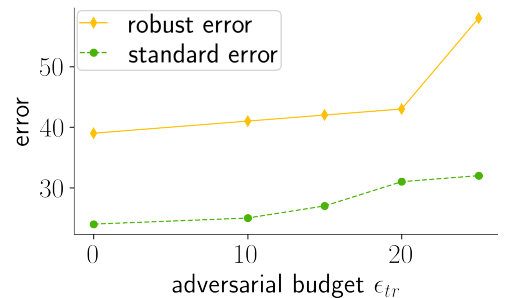


Figure 16: We plot the standard error and robust error for varying adversarial training budget ϵ_{tr} . We see that the larger ϵ_{tr} the higher the robust error.

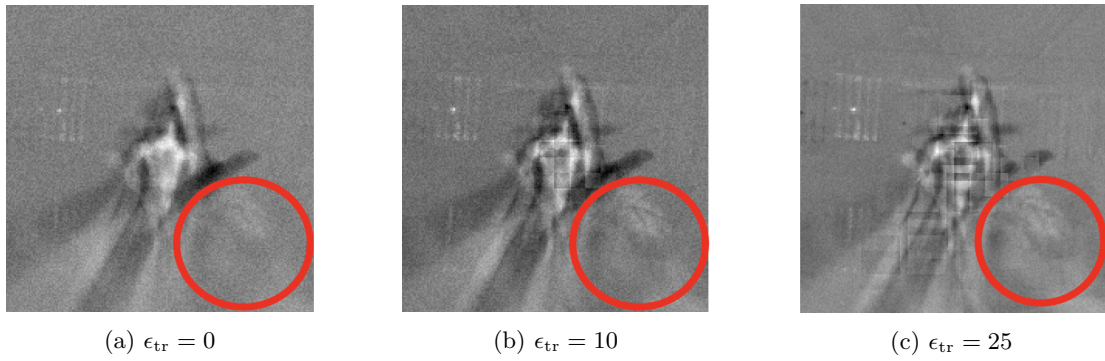


Figure 17: We visualize the logistic regression solutions. In Figure 17a we plot the vector that induces the classifier obtained after standard training. In Figure 17b and Figure 17c we plot the vector obtained after training with square-mask perturbations of size 10 and 25, respectively. We note the non-signal enhanced background correlations at the parts highlighted with the red circles in the image projection of the adversarially trained classifiers.